QUANTITATIVE VISCOELASTIC SPECTROSCOPY OF POLYMER FILMS USING LORENTZ FORCE ACTUATED CONTACT RESONANCE ATOMIC FORCE MICROSCOPY

BY

METE BAKIR

THESIS

Submitted in partial fulfillment of the requirements
for the degree of Master of Science in Mechanical Engineering
in the Graduate College of the
University of Illinois at Urbana-Champaign, 2014

Urbana, Illinois

Adviser:

Professor William Paul King

ABSTRACT

This thesis presents development of a material metrology technique, which is shown to quantify viscoelastic properties of a polymer film within the glass transition region. Designed for nanoscale material characterization applications, heater integrated atomic force microscopy (AFM) cantilever operates in contact resonance mode actuated by externally induced Lorentz force. It is demonstrated that glass transition temperature (T_g) of polymethyl methacrylate (PMMA) film can be detected reproducibly by monitoring contact resonance frequency of the cantilever as a function of temperature. Also, the glass transition temperature is observed in the terms of differential change of cantilever electrical resistance and differential power consumption. Furthermore, employing a harmonic oscillator model to define tip-sample contact interactions, viscoelastic properties of contact stiffness, viscous damping coefficient and elastic modulus for the polymer film are measured as functions of temperature. In addition, multi-frequency actuation for contact resonance is demonstrated providing qualitative material properties. Besides, a mathematical approach is developed to model two-leg and V-shaped LCR cantilevers as in the form of rectangular beam. Finally, local viscoelastic measurements taken on 66-63K PS-PMMA lamellar block copolymer film are presented. Also, nanomechanical surface property mappings of both 37-37K PS-PMMA lamellar and 46-21K PS-PMMA cylindrical block copolymer morphologies are provided. The technique introduced in this work has vast potential to be employed for numerous nano-scale material applications, and eventually replace traditional macro-scale thermophysical material characterization technologies providing local, reproducible and non-destructive analyses.

This thesis is dedicated to my family for their unending support and encouragement through my entire education life. And, to people I have met in this path who inspired, guided and helped me. "And my success is not but through Allah. Upon him I have relied, and to Him I return."

ACKNOWLEDGMENTS

I am grateful for my family, whose support and guidance has always encouraged me to pursue my dreams for higher education. I would like to acknowledge my friends and colleagues for their help and friendship provided through this work. Special thanks to my advisor, professor William Paul King, for providing me with the opportunity to work in this project and for his sage guidance. Finally, I would like to extend my thanks to Republic of Turkey Ministry of National Education for providing me scholarship to financially support my education.

TABLE OF CONTENTS

CHAPTER 1: INTRODUCTION

Investigation of material properties on the nanoscale has been enabled with invention of the atomic force microscopy [1] (AFM). In the last decade, several AFM-based thermal and mechanical metrology techniques [2-6] have been developed that provide measurements with nanometer scale resolution. Spanning emerging applications of nanocomposite materials [7-8], multiphase structures with nanoscale domains [9-10] and pharmaceuticals [11-12], the methods are pronounced to be functional tools for material characterization purposes. However, those techniques are limited to identify materials through either only thermal property measurements or mere mechanical stiffness analyses. Besides, current thermophysical material characterization technologies, such as Dynamic Mechanical Analysis (DMA), are suitable only for macro-scale material applications which preclude investigation of local dynamics of heterogeneous samples. Hence, temperature dependent analysis of mechanical material properties at the nanoscale has become an immediate requirement. This thesis describes development of a quantitative metrology technique to study local viscoelastic properties of materials in the glass transition region.

State-of-the-art techniques for nano-scale material characterization can be classified under two main domains: mechanical spectroscopy and thermal analysis. Mechanical spectroscopy methods, such as contact resonance force microscopy (CR-FM), define tip-substrate interactions through linear beam model [13] and develop constitutive equations for numerous material properties (e.g. elastic modulus, indentation modulus). CR-FM has been widely utilized to acquire topographical maps of mechanical properties on polymer surfaces [14-15]. In addition, Lorentz contact resonance method [6] (LCR), recently introduced, is a

promising imaging tool for identifying materials in a matrix based on stiffness differences. However, CR-FM and LCR-AFM have not been implemented to temperature dependent viscoelastic material measurements. Thermal analysis techniques, such as local thermal analysis with heater integrated probes [4], enable point-based measurements for the glass transition temperature of polymer films by monitoring deflection signal or electro-thermal properties of cantilever. Also, the heated probes are employed with band-excitation atomic force acoustic microscopy (BE-AFAM) technique [5,16]. BE-AFAM is demonstrated to estimate mechanical properties of polymer films as a function of temperature based on contact resonance frequency measurements. Nevertheless, BE-AFAM is not sensitive enough to display the glass transition region in the terms of mechanical properties of materials. Consequently, the published works have not used LCR-AFM technique with forced harmonic oscillator model to obtain viscoelastic properties of materials in the glass transition region.

This thesis explores development of an AFM based quantitative material metrology technique, V-Lorentz, to investigate viscoelastic properties of polymethyl methacrylate (PMMA) film in the glass transition region. It is shown that the glass transition temperature can be detected with reproducible results by monitoring response of contact resonance frequency as a function of temperature. Also, the glass transition temperature is measured in the terms of differential change of cantilever electrical resistance. Besides, it is achieved to demonstrate for the first time that differential power consumption of the cantilever discloses the glass transition region clearly, defined with three distinct temperatures, being also in agreement with DSC measurements. More importantly, responses of quality factor, contact stiffness, viscous damping coefficient and elastic modulus with respect to temperature are shown to behave in accordance with harmonic oscillator model.

CHAPTER 2: SYSTEM DESCRIPTION

2.1. Lorentz Contact Resonance Cantilevers

Figure 2.1 shows Lorentz Contact Resonance (LCR) cantilevers used in the experiments. LCR cantilevers are designed to fulfill below defined cantilever operational goals and be reconcilable with state of the art microfabrication technologies. Initially, the cantilever is aimed to be quite soft providing first mode air resonance frequency of 30 kHz and have reduced cantilever stiffness of 0.3 N/m for mechanical spectroscopy purposes. Having these properties, LCR cantilevers sustain non-destructive contact resonance operations, which is immediately required for soft materials. Then by extending segment length in free-end region of the cantilever in which Lorentz force exerts, it is enabled to achieve the highest possible Lorentz force with respect to the lowest amount of AC voltage supplied. Next, structural materials and the cantilever should be compatible with current batch fabrication techniques. Fourth, microcantilevers should be eligible to be operated in commercial AFMs.

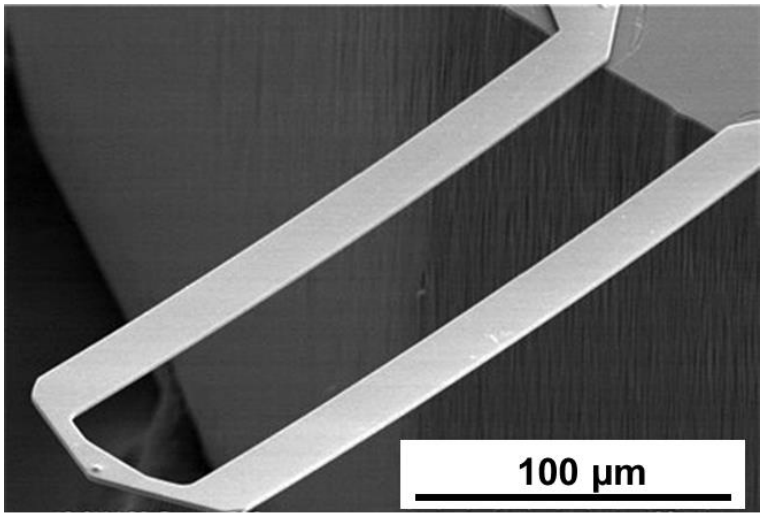

Figure 2.1 Scanning Electron Microscope (SEM) image of the LCR cantilever. The cantilever has high phosphorous doped leg regions and a low phosphorous doped heater region near the tip.

The LCR cantilevers have two major parts; high doped single crystal silicon legs that are 225 μm long, 20 μm wide and 1.5 μm thick, and low doped free end heater region. The free end region also includes a cone shaped sharp tip with 1 μm height and 20 nm radius of curvature. The cantilever used in this work has a spring constant of 0.35 N m^{-1}, and first mode air resonance frequency of 30.5 kHz. Also, the cantilever electrical resistance is 1.35 kΩ at 25 °C.

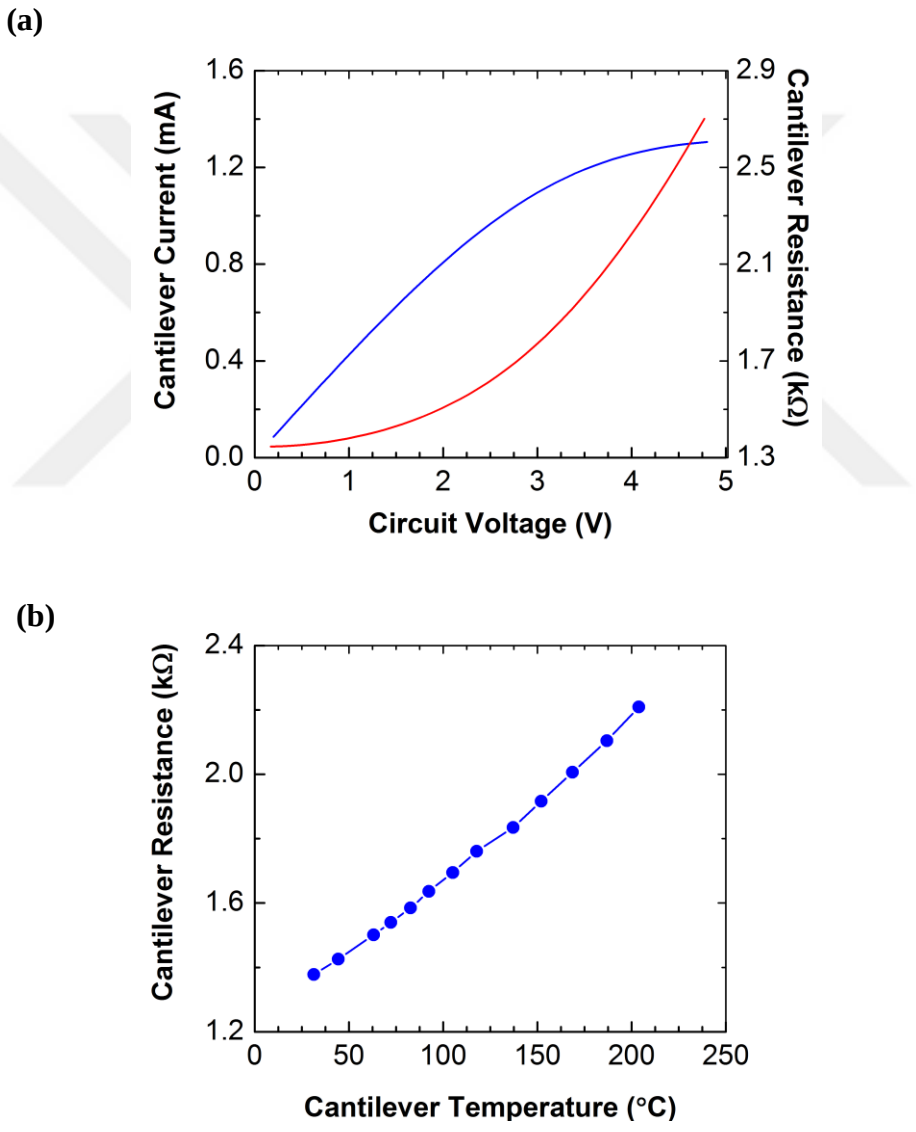

Figure 2.2 Electrical and electro-thermal characterization of LCR cantilevers. Current and resistance of the cantilever as a function of total voltage supplied to the circuit (a). Cantilever resistance as function of cantilever temperature (b).

2.2. Lorentz Force Actuation Mechanism

Lorentz force actuation for heated atomic force microscopy cantilevers is a technique that can be employed to image surface topographies and measure softening temperatures of thin polymer films [17]. Figure 2.1 shows Lorentz force actuation mechanism designed for AFM operations. Heater region integrated single crystal silicon microcantilevers are used in the Lorentz force-induced AFM operations. An oscillating current is supplied along the cantilever that interacts with magnetic field produced by a permanent magnet placed just beneath the cantilever. The interaction produces Lorentz force exerting on tip of the cantilever. The Lorentz force is governed by the equation:

$$F = l(\vec{i}x\overrightarrow{B}) \tag{1}$$

where F is the Lorentz force, l is the length of the cantilever that Lorentz force is applied, i is the alternating current and B is the magnetic field.

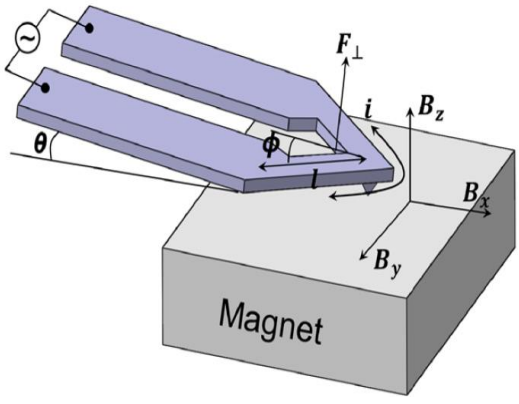

Figure 2.3 Schematic of Lorentz force actuation mechanism. A microcantilever with integrated resistive heater region is oscillated by alternating current (i) passing through the probe. A permanent magnet is placed underneath the cantilever that produces magnetic field (B) directed to the cantilever. Lorentz force (F) applies on tip of the cantilever induced by interaction of the magnetic field and the oscillating current.

2.3. Contact Resonance Operation

In conventional AFM operations, a cantilever is oscillated at such frequencies corresponding free vibrational resonance modes that are measured while out of contact. Yet, when the cantilever is placed into contact with a substrate, the vibrational frequencies shift to higher values due to interactions occurring between the tip of the cantilever and the substrate [18]. In Fig 2.3, schematics illustrate response of the cantilever being out of contact (a) and in contact (b). Also, characteristic behavior of contact resonance frequency curve in a frequency spectrum, which also includes first two modes of free resonance frequencies, is demonstrated (c).

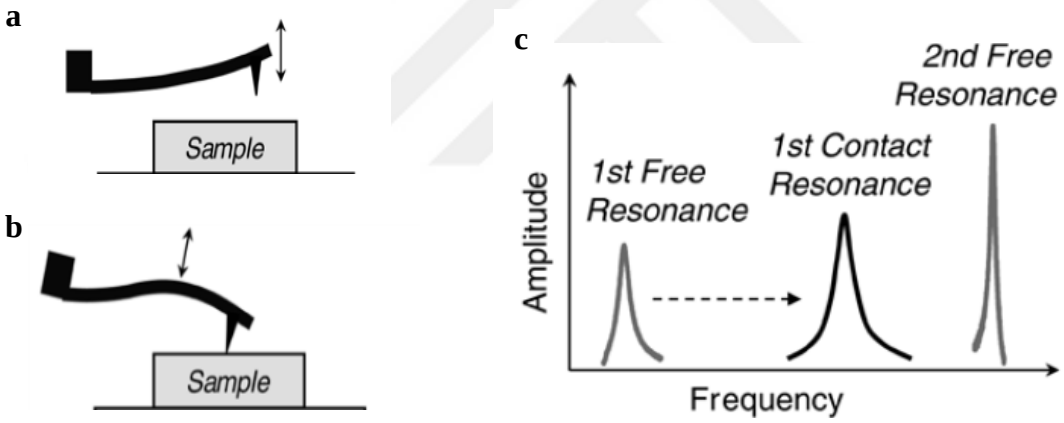

Figure 2.4 Schematics of contact resonance AFM. Resonance modes of the cantilever when oscillated in the air (a) and in contact (b). The resonance frequency spectrum (c) shows that first mode of the contact resonance frequency takes place between the first and the second modes of the free resonance oscillation.

Contact resonance force microscopy (CR-FM) goes beyond being a mere imaging technique, and is employed to measure nanomechanical properties of materials [19]. Thus, in order to acquire quantitative measurements regarding material properties, tip-surface interactions need to be defined using appropriate models.

In this regard, linear beam model [13] has been widely used to model cantilever while in contact in order to derive material properties. Figure 2.4 demonstrates a schematic of linear beam model in which cantilever is coupled with the surface. In addition to the cantilever, the contact point is then modeled as a spring and a dashpot. Based on this model, primarily a constitutive equation for contact stiffness (k^*) is obtained [20] so that simply tracking variations in the contact stiffness in a composite structure, various materials can be distinguished with respect to different stiffness values. Furthermore, contact stiffness measurements can be transformed into elastic material properties such as elastic modulus, indentation modulus and viscosity by applying contact mechanics theories [21].

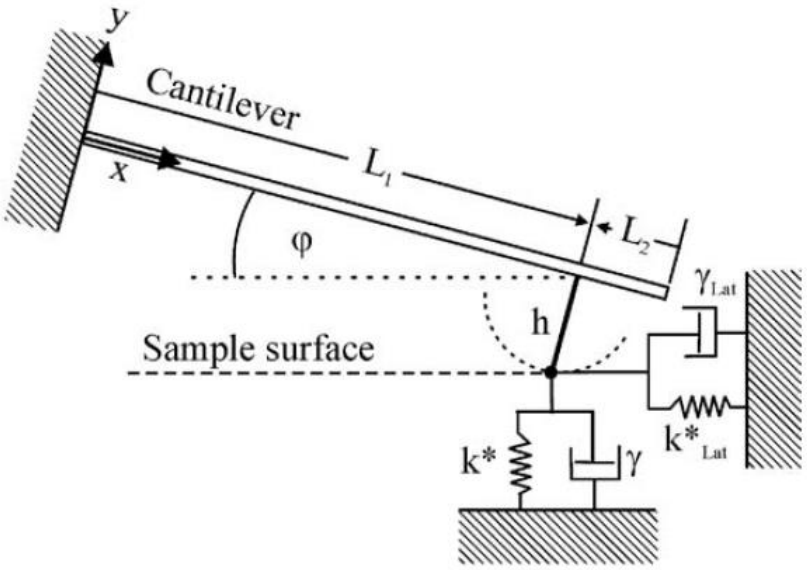

Figure 2.5 Linear model of the cantilever while the tip is in contact with the substrate. The tip-surface interactions are modeled with dashpots and springs. The cantilever is tilted by angle φ with respect to the surface. Height of the tip is *h*, located at a position L_1 on the length axis of the cantilever. The distance of the tip to the free end of the cantilever is L_2.

2.4 Lorentz Contact Resonance Operation

Contact resonance force microscopy (CR-FM) operations are widely well-known to be employed with two AFM methods: Ultrasonic Atomic Force Microscopy (UAFM) [22] and Atomic Force Acoustic Microscopy (AFAM) [23]. For both of the techniques, the oscillation to the cantilever is supplied by a piezo shaker, located either beneath the cantilever or under the substrate. However, the vibrations provided by the piezo introduce many parasitic resonances generated within the piezo system that have negative impacts on quality of the measurements. Having recently developed, Lorentz Contact Resonance Atomic Force Microscopy operation [6] (LCR-AFM) eliminates the spurious resonances providing clean and smooth frequency spectra. By doing so, LCR-AFM is pronounced to be a promising technique for nanomechanical spectroscopy of soft materials.

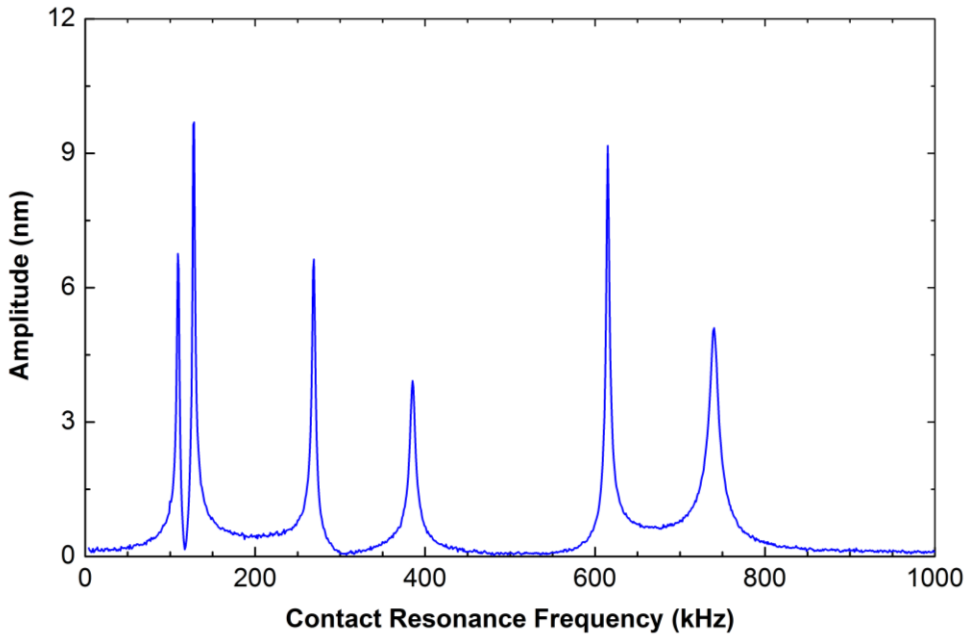

Figure 2.6 Contact resonance frequency spectrum of PS film obtained by LCR 0.3 cantilevers. Using Lorentz actuation, clean spectrum can be obtained as well as accessing higher eigenmodes.

CHAPTER 3: EXPERIMENTAL SETUP AND MODELLING

3.1 Design of Experimental Setup

As discussed in the previous chapter, LCR-AFM is the perfect combination of Lorentz force actuation mechanism and contact resonance AFM technique. In this study, we focused on point-based thermophysical measurements with LCR cantilevers. To this end, we designed an experimental setup that allows us to control temperature increase rate and take independent measurements on thin polymer films at different locations. Figure 3.1 shows experimental setup of LCR-AFM for point-based thermomechanical measurements.

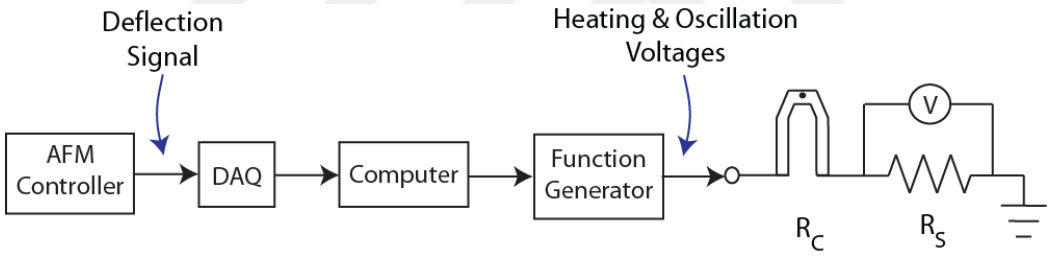

Figure 3.1 Experimental setup of LCR-AFM. The system is controlled through a Labview code on a computer. A chirp AC waveform and ramping DC voltage are sent to the cantilever. Deflection signals are collected by a DAQ board to be then transformed into frequency signal forms using FFT. Voltage drop across the sense resistor is measured to detect cantilever resistance.

The data flow of the system is governed via an in-house LabView code. The code written in LabView helps to control major equipment in the system: function generator, multimeter and data acquisition board through several key parameters: initial and final frequencies for frequency sweep range, sweep time, AC voltage, initial and final values for DC voltage for temperature ramp.

The working principle of the system is structured as following. Initially, a region of interest is defined based on contact resonance frequency spectrum (such as first mode) through inputs of above mentioned parameters. When the system is started, it initially sends AC voltage at a certain value with DC offset and sweeps the predefined frequency range. Corresponding to this external trigger, a set of deflection data is collected from the deflection channel of the AFM controller. The data from the deflection channel are grabbed through a data acquisition board (DAQ) which is also controlled via the LabView code. The collected data are then transformed into frequency spectrum form using a Fast Fourier Transform (FFT) code written in Matlab. In the frequency spectrum, it can initially easily be observed the contact resonance frequency, yet required to be exactly known peak value of the curve. In this regard, Lorentzian Curve Fitting Curve code, based on harmonic oscillator model, in Matlab is applied to determine exact values of not only contact resonance, but also quality factor. To this end, AFM signal dependent part of the system is resolved. The next step is to read voltage drop across the sense resistor to calculate electrical resistance that corresponds to that specific contact resonance frequency. By doing so, the contact resonance frequency value is matched with electrical resistance of cantilever. This procedure is followed a number of steps, which is defined by increase rate of DC voltage.

3.2 Temperature Calibration

Since temperature calibration of the heater integrated cantilevers is explained in different works [24] in great details, it is not discussed here. Yet, it is required to describe how the measured contact resonance frequencies are matched with certain temperature values. In this sense, a protocol detailed below is followed. Initially, response of cantilever electrical resistance with respect to cantilever voltage is obtained while the cantilever is kept in contact with the substrate in the AFM setup. Then for rest of the measurements, Raman spectroscopy setup is used while the cantilever is kept in the air. First, the trend of cantilever electrical resistance corresponding to cantilever voltage is acquired through voltage sourcemeter and multimeter. Second, using Raman spectroscopy, temperature of the free end region, being very close to the tip, of the cantilever is measured with respect to different cantilever voltages supplied. Third, based on the first two measurements, the temperature and the electrical resistance of the cantilever are matched. The last step is to assign the cantilever electrical resistance measured in contact with temperatures detected via Raman spectroscopy. Since the electrical resistance of the cantilever is an intrinsic property [25], matching electrical resistance and temperature holds same values regardless of being in contact or out of contact. Hence, a response curve and a definitive equation are obtained that is used to convert electrical resistance of the cantilever to temperature values. Eventually, each contact resonance frequency can be defined in the terms of temperature which then becomes important when extracting viscoelastic material properties.

3.3 Modelling of Tip-Surface Interactions

As discussed in Chapter 2, once the cantilever is brought into contact with a substrate, contact interactions take place between the tip of the cantilever and the sample. Even though the interactions have been modeled through linear beam model, the model is not convenient to be employed with cantilever beam forms different than rectangular shape. Besides, quite demanding mathematical formulations make the system depending on multi parameters and vulnerable to mistakes. To eliminate that problem, a model recently introduced [5] is used that simply eliminates dependence on cantilever geometry and provides handy equations. Figure 3.2 shows the cantilever-sample interaction model.

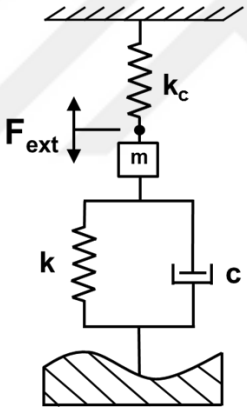

Figure 3.2 Tip sample interaction model.

The model, externally driven harmonic oscillator, basically has two major components. The upper part, with a spring and a mass, is defined as the cantilever. The lower part, with a spring and dashpot, is defined as the sample. k_c and m denote spring constant and mass of the cantilever, respectively. On the other hand, k and c indicate tip-sample contact stiffness and viscous damping coefficient of the sample, respectively. The external force being exerted on the system is the Lorentz force which oscillates the cantilever and actuates the fundamental eigenmode frequency.

For harmonic oscillator, the oscillation amplitude is defined based on the equation;

$$x = \frac{Fo/m}{\sqrt{(\omega_o - \omega)^2 + 4\gamma^2\omega^2}} \tag{2}$$

where ω and ω_0 denote excitation frequency and natural frequency of the system, respectively. F_0, m, γ and x indicate external force, mass of the system, damping coefficient and oscillation amplitude, respectively. Based on the harmonic model and the equation above, other relations can be obtained;

$$f = f_0\sqrt{1 - 1/Q^2} \tag{3}$$

where Q is the quality factor of the cantilever. Based on this equation, quality factor is anticipated to be directly proportional to contact resonance frequency.

More importantly, an approximate equation is introduced to observe contact stiffness variations with respect to change of the contact resonance frequency.

$$\omega \cong \left(1 - 5.8\frac{k_c}{k}\right)\omega_{bound} \tag{4}$$

where ω_{bound} denotes the contact resonance frequency measured on infinitely stiff material.

The same work also provides an equation for calculation of viscous damping coefficient of a sample as a function of quality factor, mass, contact stiffness and cantilever spring constant;

$$c \cong \frac{\sqrt{m(k_c + k)}}{Q}\left(2 - \frac{3}{Q}\right) \tag{5}$$

Being more importantly, elastic modulus of the sample can be calculated using Hertzian contact theory which predicts no adhesion forces take place between contacting bodies:

$$E = \frac{k}{2a} \tag{6}$$

where E and a are reducde elastic modulus and contact radius, respectively.

3.4 Thermal Resistance Network for Heat Flow

Figure 3.3 shows the thermal circuit representing heat flow from the tip to the sample and the environment [4]. Since the tip has a sharp form, it directs the heat flow to a very small contact area that makes the tip temperature (T_{int}) difficult to predict. Also, the tip temperature does strictly depend on R_{tip}, $R_{contact}$ and R_{spread} which are estimated to be on the orders of 10^6, 10^7 and 10^8 K/W. Hence, the difference of the thermal resistances causes a temperature difference between $T_{measured}$ and T_{tip}. This fact will become important when analyzing results.

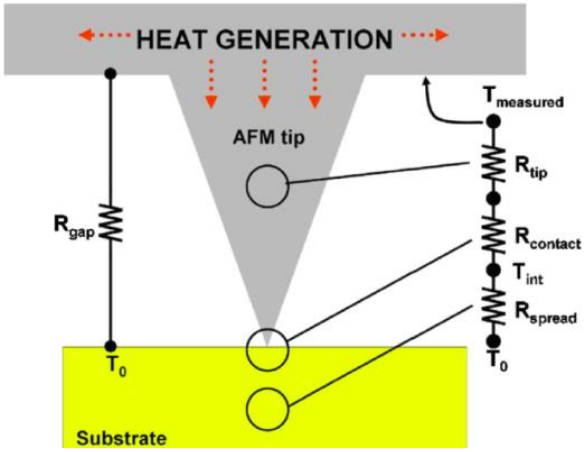

Figure 3.3 Thermal circuit network of tip-sample contact. Heat transfer occurs to the substrate and the environment. Temperature of the tip becomes different than the measured temperature due to difference in magnitudes of R_{tip}, $R_{contact}$ and R_{spread}.

CHAPTER 4: VISCOELASTIC ANALYSIS OF PMMA

4.1 Probing Glass Transition Temperature

Figure 4.1 demonstrates response of contact resonance frequency as a function temperature. It is shown three independent measurements taken on a thin PMMA film from different locations, and obtained reproducible results. In the experiments, total circuit AC voltage is set to 1.0 V and the frequency is swept between 120 kHz and 150 kHz. Deflection signal set point voltage in AFM is set to 1.0 V that corresponds to approximately 300 nN static force exerting on the cantilever. DC voltage is ramped from 2.5 V up to 4.0 V by 0.1V increments. Temperature increase rate of the system is approximately 6˚C/s. It is observed that the contact resonance frequency increases steeply starting right after 80 ˚C, and reaches a peak point, which happens around 151˚C, and then decreases as the temperature is kept elevated. The glass transition temperature is the peak point that the contact resonance frequency curve shifts its trend. The average glass transition temperature measured is 151.2˚C.

The observed increasing trend of the contact frequency curve can be attributed to several reasons. One possible cause is that contact area between the tip and the sample enlarges due to thermal expansion of the glassy material [26]. The other option could be reorganization of the polymer structure into a stiffer morphology just before the glass transition occurs [27]. Another reason might be stemming from lateral tip-sample forces which indeed elevate the contact resonance frequency [28].

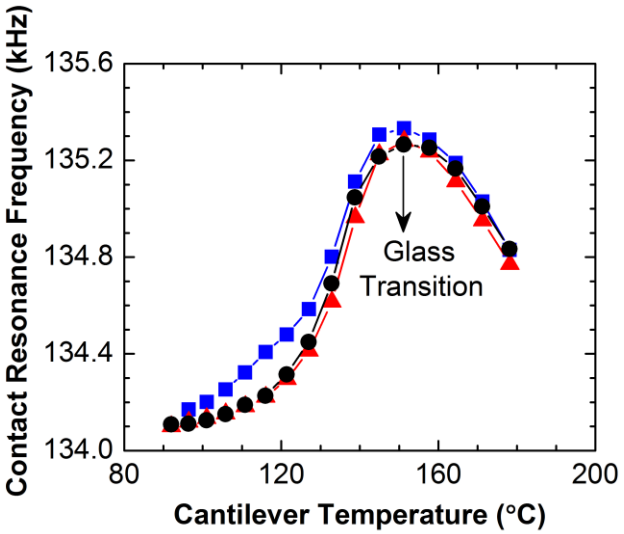

Figure 4.1 Contact resonance frequencies as a function of probe heater temperature on PMMA film. The contact resonance frequency rises up until the glass transition temperature, and then shows a clear drop when the tip of the cantilever starts sinking into the material after the peak point.

Another way to detect the glass transition temperature is to observe differential change of cantilever electrical resistance with respect to temperature increments. Being different from the frequency measurements, the cantilever electrical resistance rises up while the temperature is increased until the thermal runaway point, which happens around 500-600˚C [24]. Unfortunately, it is difficult to observe the glass transition phenomena just tracking the electrical resistance. Yet, response of differential incremental rates of the electrical resistance yields a small 'plateau' region, in which the glass transition temperature is observed. Same parameters used in the contact resonance frequency measurements are also valid for differential electrical resistance measurements. The measured glass transition temperature is 153.2˚C.

Thermal transport mechanism, shown in Fig. 3.3 helps to understand the response of cantilever electrical resistance at the glass transition temperature. Initially, the temperature of the tip (T_{tip}) is below the glass transition temperature of the PMMA film. And, while the temperature

of the cantilever is increased, it then causes electrical resistance of the cantilever to rise up. When the tip temperature reaches to the glass transition temperature, the tip slightly sinks into the material which is observed as decrease in the thermal impedance between the tip and the substrate. The drop of the thermal impedance reflects upon the electrical resistance of the cantilever, and causes it remain constant for a short temperature range. This constant response is monitored as the flat region in Fig. 4.2

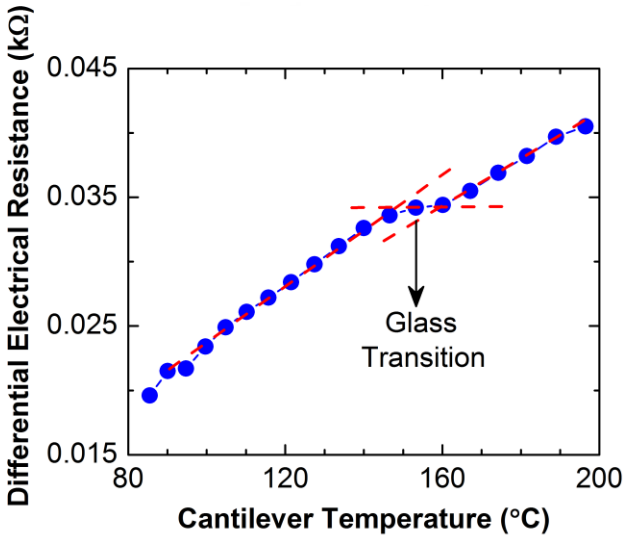

Figure 4.2 Differential increase of the cantilever electrical resistance as a function of probe heater temperature. Decreased thermal impedance causes constant response in the terms of differential electrical resistance of the cantilever. The flat region indicates the glass transition.

Also, the glass transition phenomenon is monitored in the terms of differential power consumption of the cantilever. The experimental parameters are the same of the above mentioned measurements. In Fig. 4.3, it is clear that the differential power consumption curve demonstrates three distinct points, which are indeed defines the glass transition region [29]. The curve has a constant slope, first, prior to the 'onset temperature', which is the point that indicates beginning of the glass transition region. The measured onset temperature is 132.8˚C. Then the slope of the

curve moves to a lower, yet constant value. This, second slope continues until the ‘peak point’ in which the glass transition temperature is observed. The temperature of the peak point is 157.7 ˚C. The last part of the curve spans the peak point and the ‘end point’. The end point specifies the ending of the glass transition region. The temperature measured at the end point is 164.3˚C. The display of the glass transition region is the first time observed in AFM measurements.

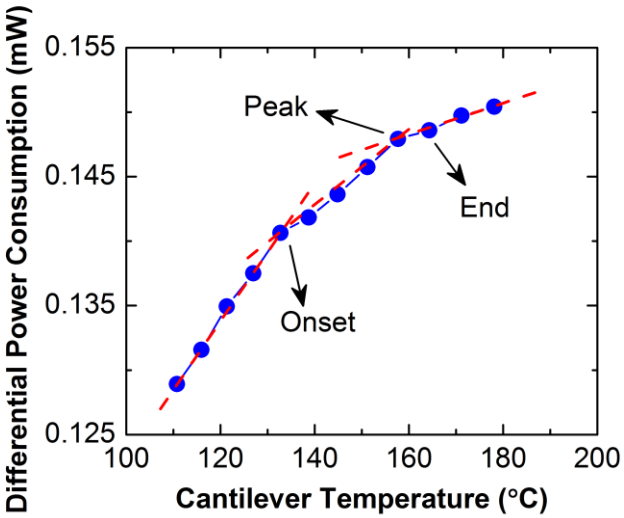

Figure 4.3 Differential power consumption of the cantilever as a function of probe heater temperature. The glass transition region is observed with three distinct points: onset, peak and end temperatures. The slope of the response curve is monitored to change at each of these points.

To validate the glass transition region observed in differential power consumption of the cantilever, we have measured the glass transition temperature of the same PMMA film using Differential Scanning Calorimetry (DSC). The experiments with DSC are done through endothermic analysis with 30˚C/min temperature increase rate. Being similar to what is measured with the AFM analyses, the three points, onset, peak and end, are observed. It is also quite obvious that trend of the heat flow curve has three different slopes changing at the distinct points of the glass transition region. The measured temperatures of onset, peak and end points

are 115.5˚C, 116.6˚C and 117.7˚C, respectively. The difference between the temperatures observed with the cantilever happens due to two facts. First, as discussed in part 3.4, the calibrated temperature the cantilever is different from the temperature of the tip. Second, different temperature increase rates of DSC and LTA cause different structure relaxations for the material [30]. Hence, even though the temperatures are different for two methods, the trends are the quite similar.

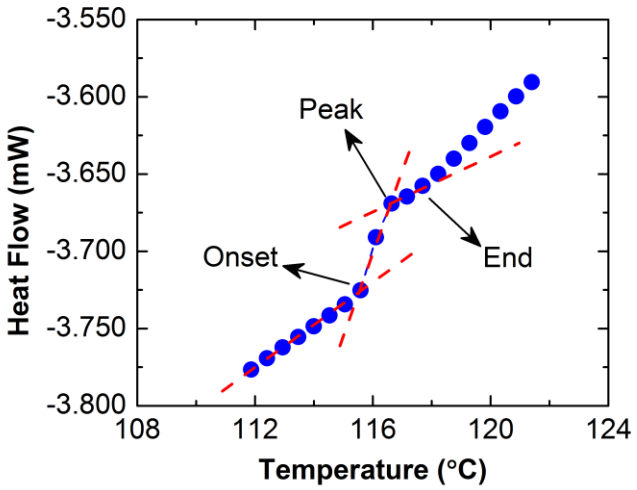

Figure 4.4 Differential Scanning Calorimetry (DSC) thermogram of PMMA film. The glass transition region is observed displayed by the three definitive temperatures: onset, peak and end. The slope of the heat flow curve varies point basis within the glass transition region.

4.2 Viscoelastic Properties in the Glass Transition Region

In Figure 4.5, quality factor of the cantilever is monitored as a function of cantilever temperature. The results of three measurements shown for quality factor are extracted from the dataset of the contact resonance frequency measurements using simple harmonic oscillator model in Matlab. The curves behave in accordance with presented theory that Equation 3 predicts quality factor to react proportional to the frequency. In other words, when the contact resonance frequency increases, so does the quality factor. As shown in Figure 4.1, the curves of contact resonance frequency have a positive slope that the frequency increases with respect to the temperature rise. Here, the quality factor exhibits similar trend having a very slight positive slope right up to the glass transition region, and then declining with increased temperature.

Furthermore, the behavior of quality factor can also be interpreted by extending its definition. The quality factor is formulated as ratio of stored energy to dissipated energy in a system. Thus, when temperature of the material is increased to the glass transition temperature, the material becomes softened that causes more dissipation energy to be transferred to the material. Eventually, the quality factor steeply goes down corresponding more dissipation energy transmitted to the material at higher temperatures. This argument is also in great agreement with effects of viscous damping coefficient, Fig 4.7.

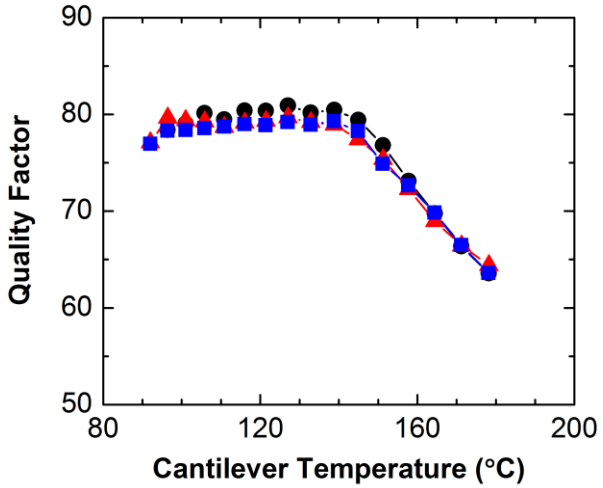

Figure 4.5 Quality factor of the cantilever as a function of cantilever temperature. Three regions are observed to describe behavior of polymer: Glassy, viscoelastic and rubbery. The glassy region shows a gentle positive slope with respect to increase of contact resonance frequency. The curves acquire negative slope starting in glass transition region. Reduced quality factor is sign of reduced dissipation energy.

Figure 4.6 shows response of contact stiffness as a function of cantilever temperature. Results of contact stiffness are derived based on dataset of the contact resonance frequency measurements using Eq.4. Yet, the equation is modified in such a way that term of contact resonance frequencies ratio ($\omega/\ \omega_o$) is switched to quality factor term, as indicated in Eq.3. By doing so, the contact stiffness is tracked as a function of quality factor.

Trend of contact stiffness is observed to remain almost constant within glassy elastic region, and starts decreasing when the temperature reaches the lower limit of glass transition region, and continues in that fashion. Unfortunately, we are not able to obtain enough data regarding rubbery region due to deep penetration happens at higher temperatures hindering cantilever vibrations and signal collection. Since the contact stiffness in fact describes the response of material, these results pave the way going through measurements of elastic modulus of material.

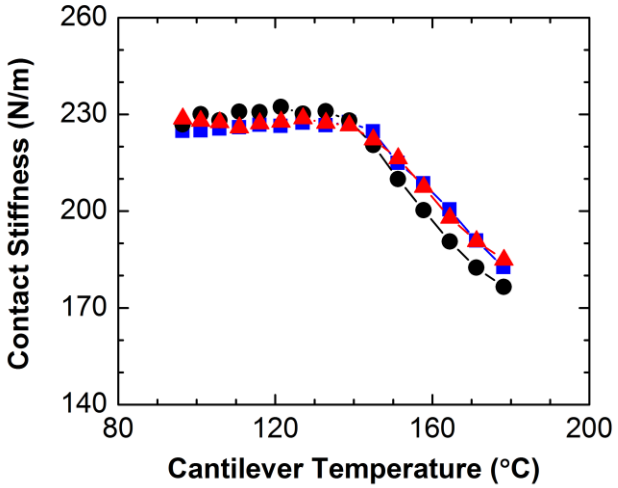

Figure 4.6 Contact stiffness of PMMA as a function of cantilever temperature. The contact stiffness has almost constant value in glassy region, whereas it declines with a constant negative slope starting in glass transition region.

Figure 4.7 exhibits how viscous damping coefficient of PMMA film reacts with respect to stepwise increase of cantilever temperature. The dataset of contact resonance frequency measurements are used here to obtain viscosity curves, employing also Eq.5. In that equation, k_1 and m terms are used as 0.35 N/m and 2.2×10^{-9} kg [5]. And, terms of k_2 and Q are taken from the temperature based measurements, shown previously. On the contrary of the contact stiffness curves, viscosity remains constant in the glassy region, and goes up dramatically in the glass transition region.

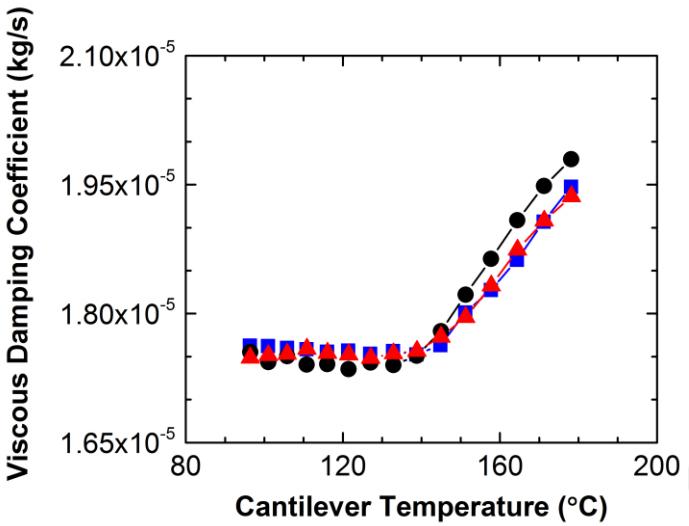

Figure 4.7 Viscous damping coefficient of PMMA film as a function of cantilever temperature. Viscosity has almost constant value in the glassy region, and then dramatically inclines in the glass transition region. Trends of the curves show that viscous terms become effective in viscoelastic region.

In Figure 4.8, it is shown elastic modulus of PMMA film as a function of cantilever temperature. Elastic modulus is calculated employing Eq.6 and using dataset of contact resonance frequency measurements. In Eq.6, contact diameter is assumed to be 100 nm, and contact stiffness values are taken from previously discussed contact stiffness measurements. The results are in harmony with what is expected that the elastic modulus is assumed to remain constant within glassy region, since contact stiffness and viscous damping are also constant. After that the elastic modulus drops in the glass transition region as also explained in the terms of contact stiffness and viscous damping coefficient. In other words, when the material becomes softened starting with the glass transition temperature, the chains of molecules in polymer structure relaxes and yields abruptly reducing eventually the elastic modulus of the structure. The results here are promising for the future that AFM with heated probes can replace state of the art technology of dynamical mechanical analysis at macroscale.

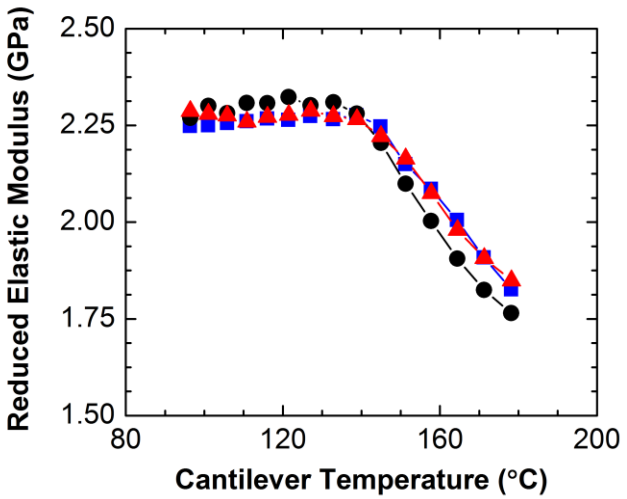

Figure 4.8 Elastic modulus of PMMA as a function of cantilever heater temperature. Elastic modulus has almost constant value within glassy region, and then dramatically falls with glass transition.

4.3 Topography of Indentation Crater

In Figure 4.9, it is shown topography of crater mark (a) left after local thermal analysis done on PMMA surface and profile of (b). The diameter of the hole is 1.6 µm at the largest side, and around 1.0 µm when measured in the axis of the surface. Height of the hole is 0.8 µm at maximum. Even though the scale of the diameter seems a little bit large for nanoscale measurements, experiments show that the best resolution for the diameter can be obtained as just below 1.0 µm. Also, it should be noted that the size of the diameter depends upon structural properties of materials. For example, if a material relaxes slowly in the glass transition region, the glass transition temperature can be detected leaving smaller craters on the surface. On the other hand, if another material yields very quickly, deformation has to be significant to observe glass transition temperature and viscoelastic properties in glass transition region.

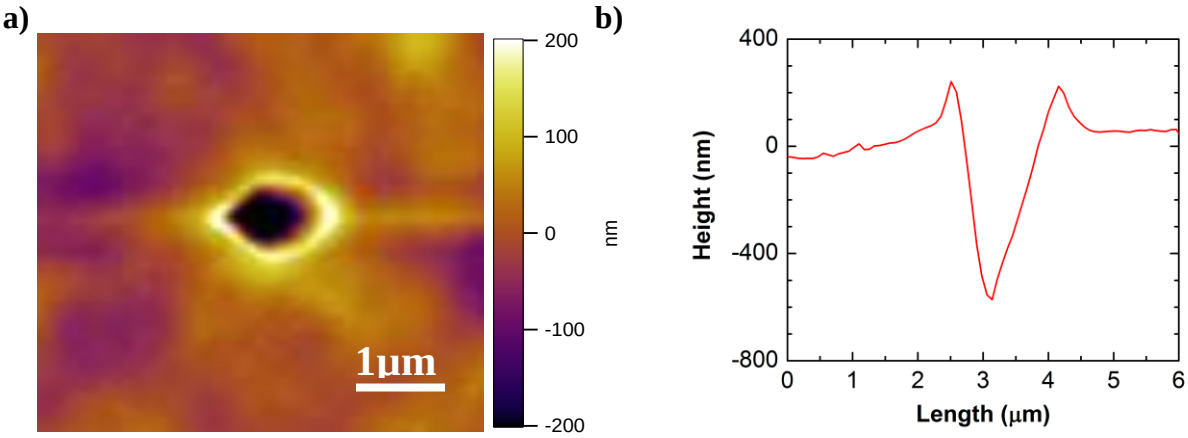

Figure 4.9 Topography of indentation crater left (a) and indentation hole profile (b).

CHAPTER 5: MULTI FREQUENCY ACTUATION

5.1. Multi-Frequency Contact Resonance Technique

Having initiated with surface-coupled cantilever theory, developed by U. Rabe [13], and then well established through numerous applications by D. C. Hurley [14,15,18], Contact Resonance Force Microscopy (CR-FM) has been demonstrated as an effective tool for surface characterization of mechanical properties on the nanoscale. To date, the published works have implemented CR-FM to Ultrasonic Atomic Force Microscopy (UAFM) [22] and Atomic Force Acoustic Microscopy (AFAM) [23] techniques. Also, Lorentz contact resonance AFM (LCR-AFM) has recently been introduced to be an alternative technique for mechanical property analysis of composite materials. [6]. In addition, several works have been produced recently coupling multi-frequency AFM operation with contact resonance technique, yet they are in lack of imaging capability [21] or application to two fundamental resonance frequencies [31], or excitation mechanism through only contact resonance mode [32] .Taken together, the state of the art methods offer CR-AFM confined to either single mode excitation of cantilever, or not fully comprehensive bimodal actuations.

However, no one has presented application of excitation of two contact fundamental resonance modes through a single contact resonance actuation mechanism. Here, we propose to combine contact resonance technique with multi-frequency excitation of cantilevers through Lorentz actuation technique. Through a successful implementation of LCR MF-AFM, we aim to develop a future promising tool for mechanical material investigation at the nanoscale providing measurements with high resolution, more sensitivity and applicable various materials morphologies.

5.2. Point-based Contact Resonance Measurements

Figure 5.2 shows the design of experimental setup for point-based multi-frequency contact resonance measurements. The experimental setup is designed in such a way that dual frequency actuation is provided through the AFM Controller. The output channel of the AFM controller basically sends two signals (f_1 and f_2) at different frequencies and different amplitudes to the cantilever, mixing them while minimizing possible attenuations may happen. Showing different responses to these two different frequencies, deflection signal collected from the AFM controller is split into two to be connected to two lock-in amplifiers. The two lock-in amplifiers are set to frequencies corresponding to two eigenmodes of the cantilever. Using this experimental setup with the lock-in amplifiers, it is possible to acquire data of amplitude, phase and quality factor of each eigenmode that cantilever is oscillated.

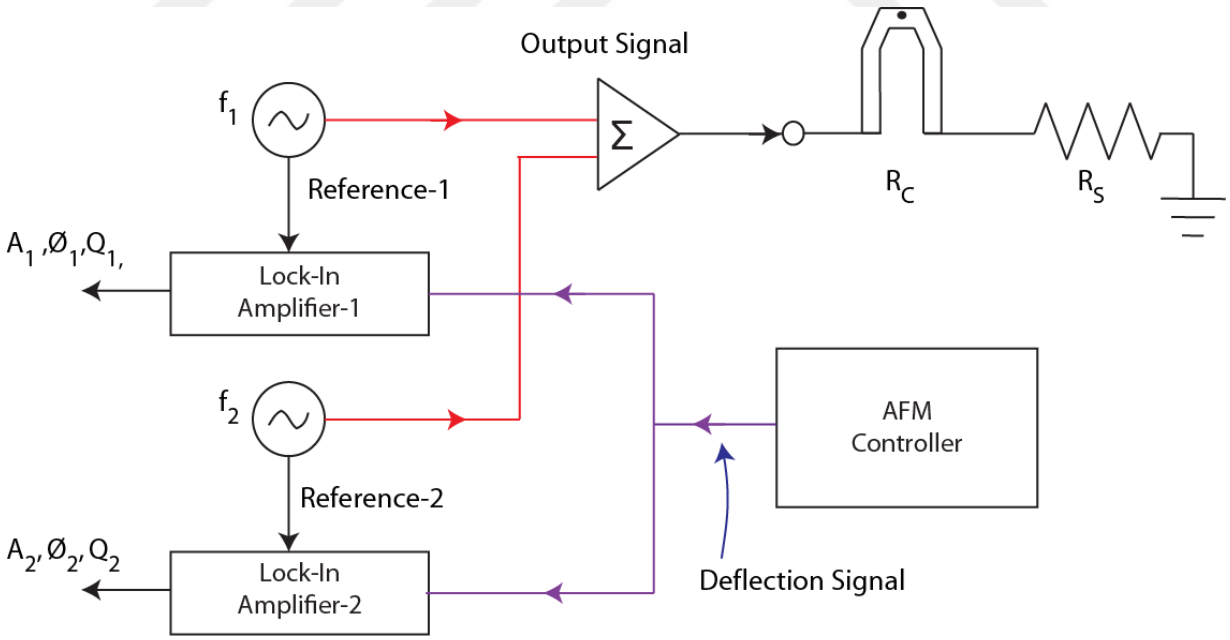

Figure 5.1 Experimental setup for point-based multi frequency contact resonance measurements. Two signals (f_1 and f_2) at different frequencies and amplitudes are sent to the cantilever. Collected deflection signal is separated and sent to the lock-in amplifiers. Data regarding frequency, amplitude, phase and quality factor can then be obtained from the lock-in amplifiers.

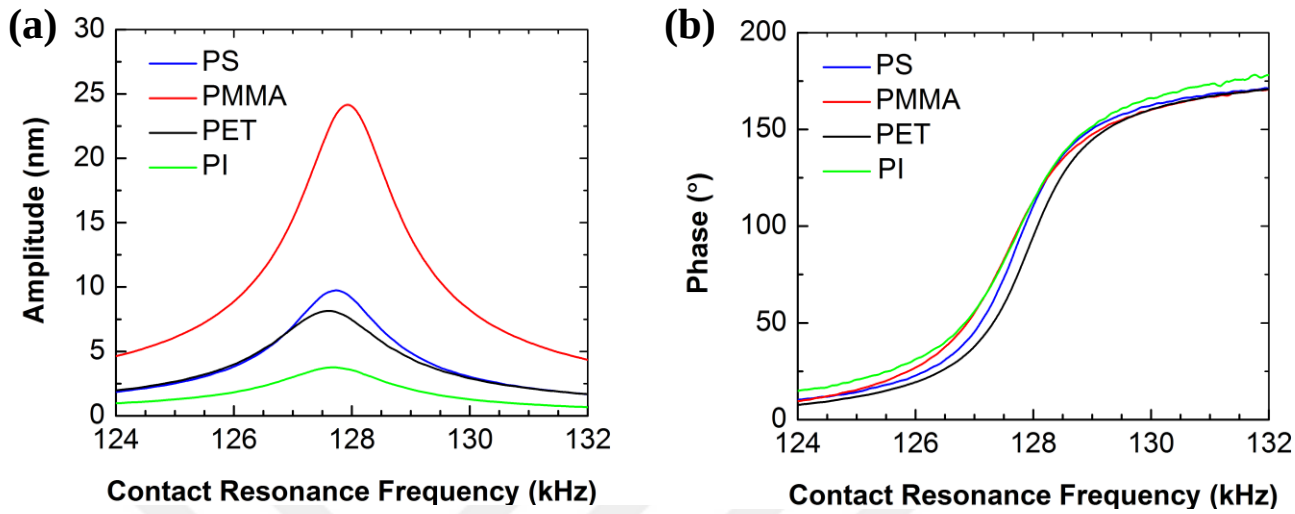

(c)

	PMMA	PET	PI	PS
f(kHz)	128.03	127.66	127.72	127.77
Φ(°)	90	90	90	90
Q	86.50	72.17	75.13	87.60
Amp(nm)	24.24	8.29	3.76	9.80

Figure 5.2 1st Mode Frequency response curves (a), phase curves (a) and averaged results of 3 independent measurements (c) taken on four different polymer films. During the measurements, applied AC voltage is 1V and tuning time is 2 seconds.

In Figure 5.2, frequency and phase curves of the 1st eigenmode obtained on different polymer films are shown. According to the figures, very slight differences in the contact resonance frequencies are observed, approximately on the order of 0.2 kHz. The phase of the 1st mode is set to 90˚ for all of the samples so that phase response for the other eigenmodes can fairly be compared. During the measurements no additional heating is applied to the cantilever, and possible heating may occur due AC voltage are ignored due to high frequency values. Also,

it is noteworthy that no such dramatic differences are observed with 2nd and 4th eigenmodes, so any figures regarding those are not provided here.

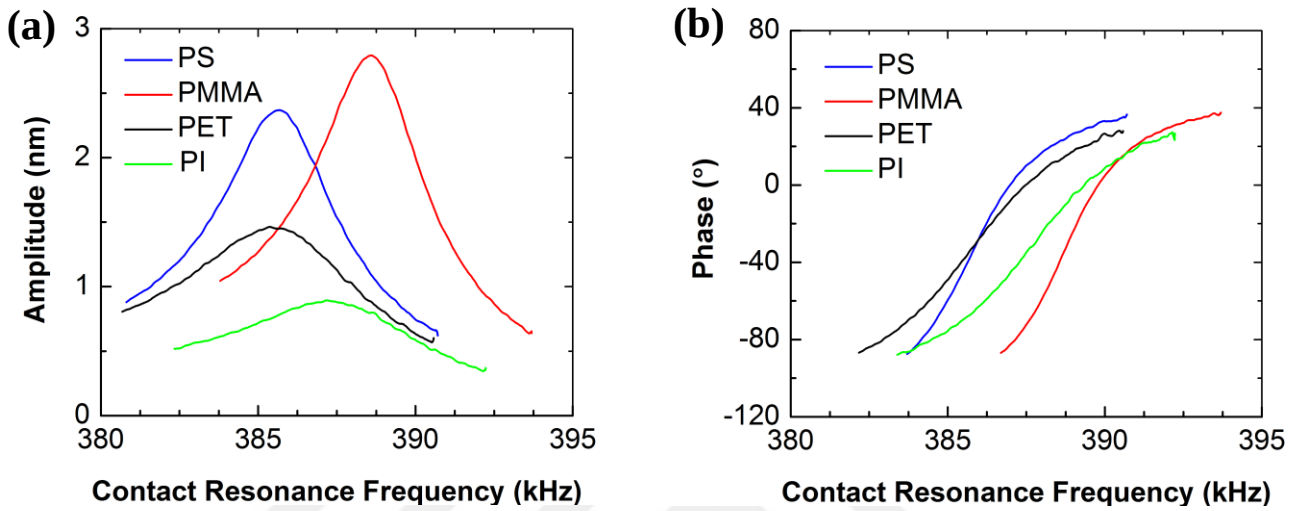

(c)

	PMMA	PET	PI	PS
f(kHz)	388.80	385.44	387.10	385.53
Φ(°)	-40.69	-41.48	-45.55	-41.85
Q	130.47	77.67	79.47	116.77
Amp(nm)	2.82	1.49	0.97	2.42

Figure 5.3 3rd Mode Frequency response curves (a), phase curves (a) and averaged results of 3 independent measurements (c) taken on four different polymer films. During the measurements, the 1st mode is kept at 1V while the 3rd mode is kept at 0.75V.

According to Figure 5.3, comparatively larger frequency shifts are observed which can be attributed to increased sensitivity of the higher mode. Being differently, very small changes in phase values are observed. Using this mode, various polymer films with different mechanical properties can be easily distinguished in the terms of amplitude, frequency and phase.

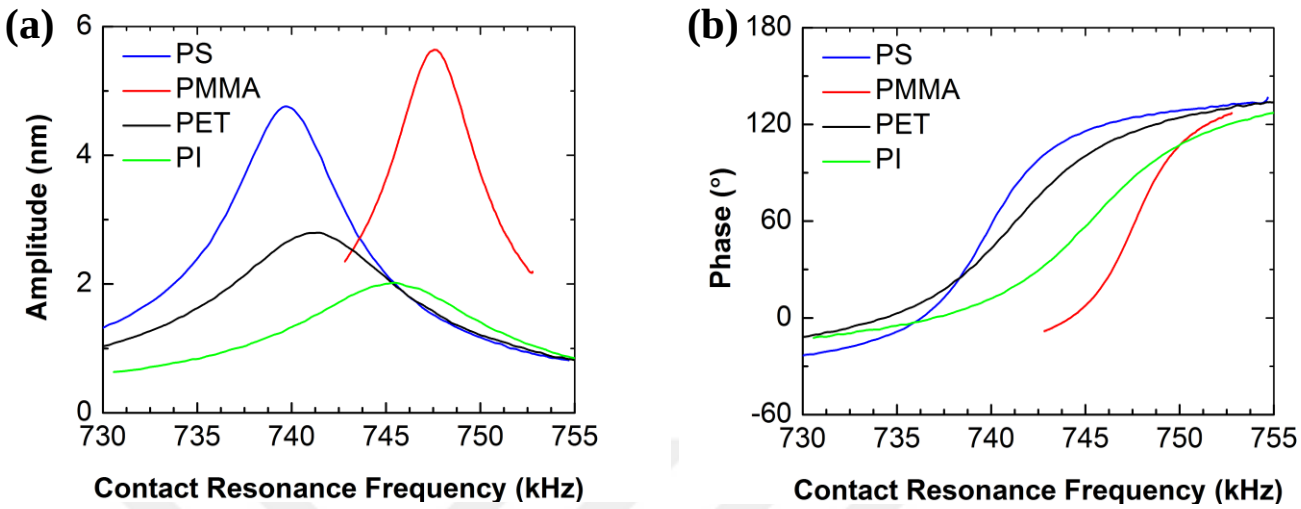

(c)

	PMMA	PET	PI	PS
f(kHz)	747.57	741.84	745.67	739.89
Φ(°)	56.48	61.24	61.87	50.30
Q	177.8	89.93	84.93	135.9
Amp(nm)	5.697	1.488	2.868	2.076

Figure 5.4 5th Mode Frequency response curves (a), phase curves (a) and averaged results of 3 independent measurements (c) taken on four different polymer films. During the measurements, the 1st mode is kept at 1V while the 5th mode is kept at 0.5V.

In Figure 5.4, it is achieved to acquire the largest frequency shifts with respect to different polymers, which is around 8 kHz. Also, there are significant differences in other definitive properties of amplitude, phase and quality factor. This mode offers promising results to be implemented into multi-frequency technique.

5.3. Surface Mapping

A complex material having components with different mechanical properties can be imaged using phase-locked loop implemented contact resonance technique. As shown in Figure 5.5, the output channel of the AFM controller is used to provide actuation signal of the fundamental eigenmode (1st mode). Also, PLL Controller is then set automatically to the higher eigenmode that the signals of two eigenmodes are mixed using a power combiner. Afterwards, the mixed signal is directed to the cantilever as a multi-frequency actuation voltage. Data regarding the response of the cantilever is collected through deflection channel, yet it contains information regarding the first and the higher eigenmodes. Thus, a signal filter is used to remove the first mode so that the PLL can circulate a loop according to the higher eigenmode. Following this, amplitude, phase and frequency output channels from the PLL detector is plugged into Input channels on the AFM controller. Hence, using AFM software itself, surface mappings of those properties can be acquired.

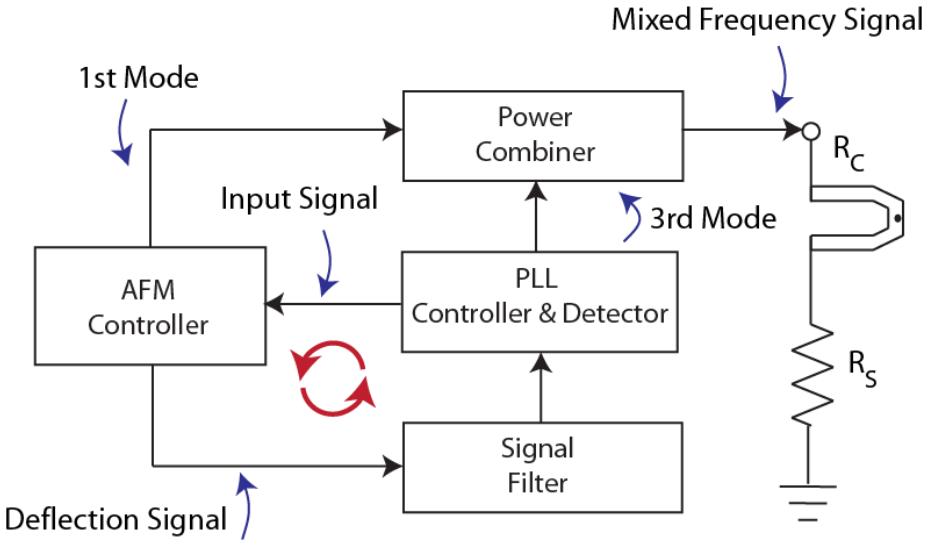

Figure 5.5 Experimental setup design for surface mapping with multi-frequency contact resonance technique. Phase-locked loop is set to higher eigenmode whereas AFM controller provides the signal of first fundamental frequency. Collected deflection signal is separated using signal filter.

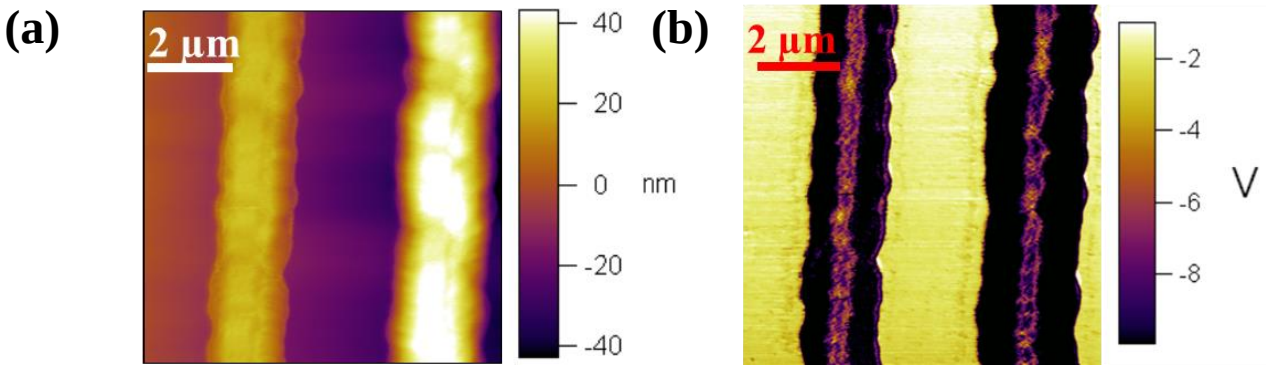

Figure 5.6 Surface topography image (a) and contact resonance frequency map (b) of PMMA-Si E-jet printed substrate. Surface topography image is obtained using the fundamental eigenmode controlled through the AFM controller, and the frequency map is acquired through the PLL. Grabbed frequency data is classified thorough voltages that can be later translated into frequency form.

In Figure 5.6, it is shown that surface topography and frequency shift on the sample can be tracked simultaneously using two different eigenmodes. The information regarding the contact resonance frequency map can be later used appropriate mathematical models to turn frequency data into quantitative viscoelastic material properties.

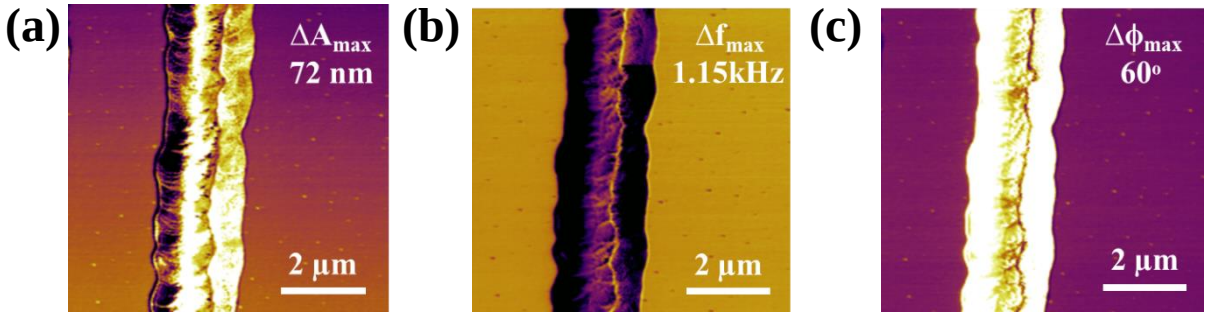

Figure 5.7 Surface maps of amplitude (a), frequency (b) and phase (c) obtained on the PMMA-Si e-jet printed substrate using fundamental eigenmode. Clear differences are observed in all the properties. The max differences of amplitude are 72nm, frequency 1.15 kHz and phase 60˚.

CHAPTER 6: MATHEMATICAL MODELING

6.1. Lorentz Contact Resonance Cantilevers

It is here presented an approach to transform Lorentz contact resonance (LCR) cantilever geometrical shape into an equivalent rectangular beam form. In other words, LCR cantilevers are modelled as if they have rectangular beam form with calculated dimensions. By doing so, the two-leg LCR cantilevers can easily fit into Euler Linear Beam Theory. Afterwards, quantitative mechanical properties of numerous materials can be acquired using this theory. In Figure 6.1 it is demonstrated a design sketch of LCR cantilevers. The legs are around 225 µm in length and 20 µm in width. There is 50 µm between the two legs. The heater region has a V-shaped form that is in 6 µm width and 17 µm length. Thickness of the cantilever is 1.5 µm.

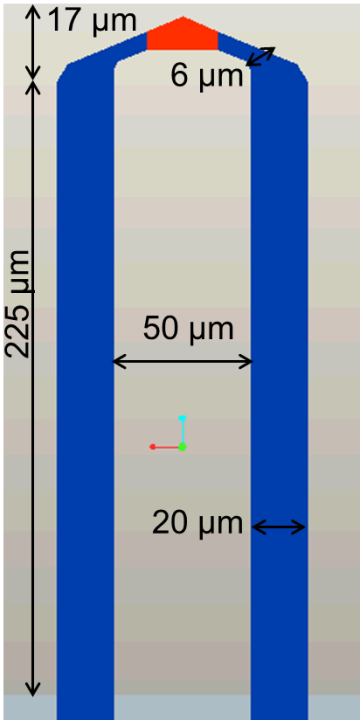

Figure 6.1 2-D sketch of LCR cantilevers. The legs are in 225 µm length and 20 µm width. Heater region has a V-shaped form.

6.2. Equivalent Cantilever Beam Model

To obtain an equivalent beam model, the LCR cantilever is split into two parts, legs and the free-end region. The stiffness of each part is calculated independently. In other words, by employing solid mechanics theory for clamped-free end beam and simulation analyses, equivalent rectangular beam forms having same particular stiffness values for each of the section are acquired. Finally, combining two-parts together in the form of single rectangular beam form, an equivalent rectangular beam model and corresponding dimensions are obtained.

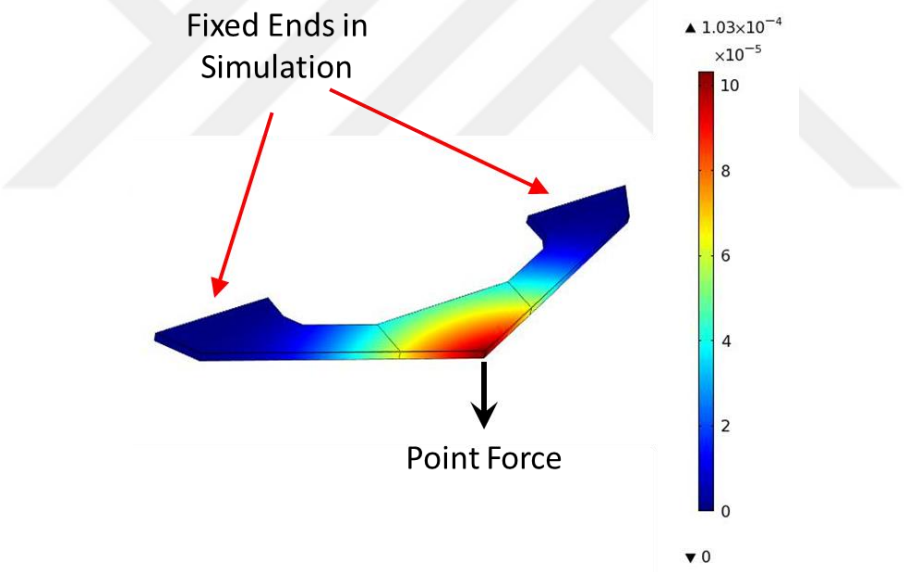

Figure 6.2 Free-end region of LCR cantilever used for stiffness calculation in COMSOL. Used parameters for Young's Modulus 169 GPa, applied force 10 nN. Computed stiffness is 97N/m.

The stiffness of the free-end region is first computed using COMSOL finite element analysis. Obtained max deflection in the simulation results is 10.3 nm and spring constant is 97 N/m. Following the FEA, the spring constant of the free-end region is also calculated employing an analytical approach [33].

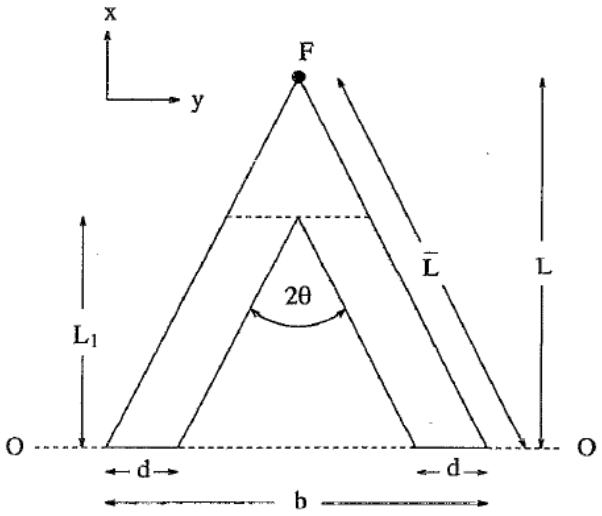

Figure 6.3 Analytical approach to obtain equivalent stiffness of V-shaped cantilever [33]. Used parameters are E=169 GPa, t=1.5 µm, L=24 µm, Θ=67.5˚, b= 90 µm and d= 12.1 µm.

$$k = \frac{Et^3 d}{2L^3} cos\Theta \left[1 + \frac{4d^3}{b^3}(3cos\Theta - 2)\right]^{-1} \quad [7]$$

Since the free-end region of the cantilever has fairly complex structure when compared to the ideal V-shaped model, d is estimated as 12.1 µm. Other dimensions are directly taken from the LCR geometry. Calculated stiffness is 96.3 N/m. There is a great agreement between the computed and calculated values using FEA and analytical approaches. Then based on the obtained stiffness values, we can design a new rectangular beam form having equivalent stiffness of the free-end region with the desired dimensions. The new dimensions are 32 µm in width, 1.5 µm in thickness, 36.18 µm in length. Using the analytical approach, equivalent stiffness value for the cantilever legs is also obtained. The calculated stiffness is 0.5357 N/m for two legs. Then the obtained equivalent rectangular beam form for the legs has 32 µm width, 1.5 µm thickness and 204.23 µm length.

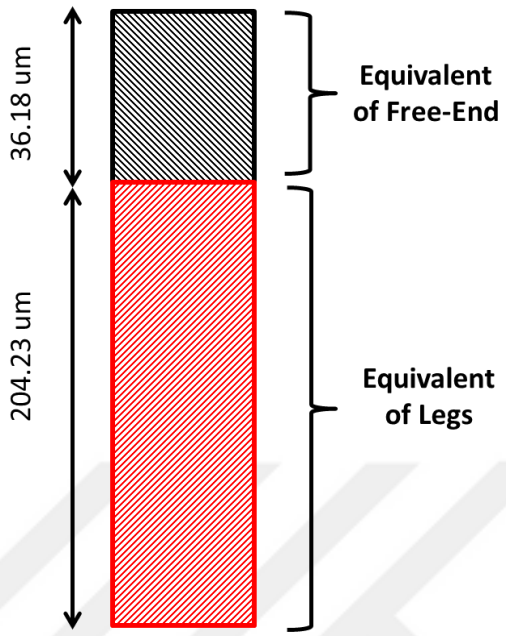

Figure 6.4 Equivalent rectangular beam form for the LCR cantilevers. Stiffnesses for free-end region and the legs are calculated using analytical and numerical approaches. Calculated overall stiffness of the new form is 0.331 N/m obtained with linear beam model and 0.384 N/m obtained with COMSOL.

Combining previously constructed equivalent beam forms of both free-end and legs, a new one-end-clamped and one-end-free rectangular beam model can be structured (Figure 6.4). The calculated stiffness of the model using linear beam equation is 0.331 N/m. The computed stiffness of the model in COMSOL is 0.333 N/m. The computed stiffness of the LCR cantilever in COMSOL is 0.384 N/m.Also, the measured stiffness of LCR cantilevers using thermal method in AFM is 0.35 N/m. There is a small discrepancy between spring constants of the LCR and the equivalent beam model which might either be stemming from complexity of the initial LCR model that approximations underestimates some details or incapability of the designed analytical method to be applied on such two-leg cantilever. Yet, we can obtain very close results that cannot obstruct using this method to model LCR cantilever.

6.3. Eigenmode Analyses

In order to provide a comprenhesive approach to obtain an equivalent rectangular beam shape, the new rectangular beam form should be in harmony with the eigenmodes of the original LCR design. In this regard, eigenmodes and eigenvalues of both forms are investigated using COMSOL finite element analysis.

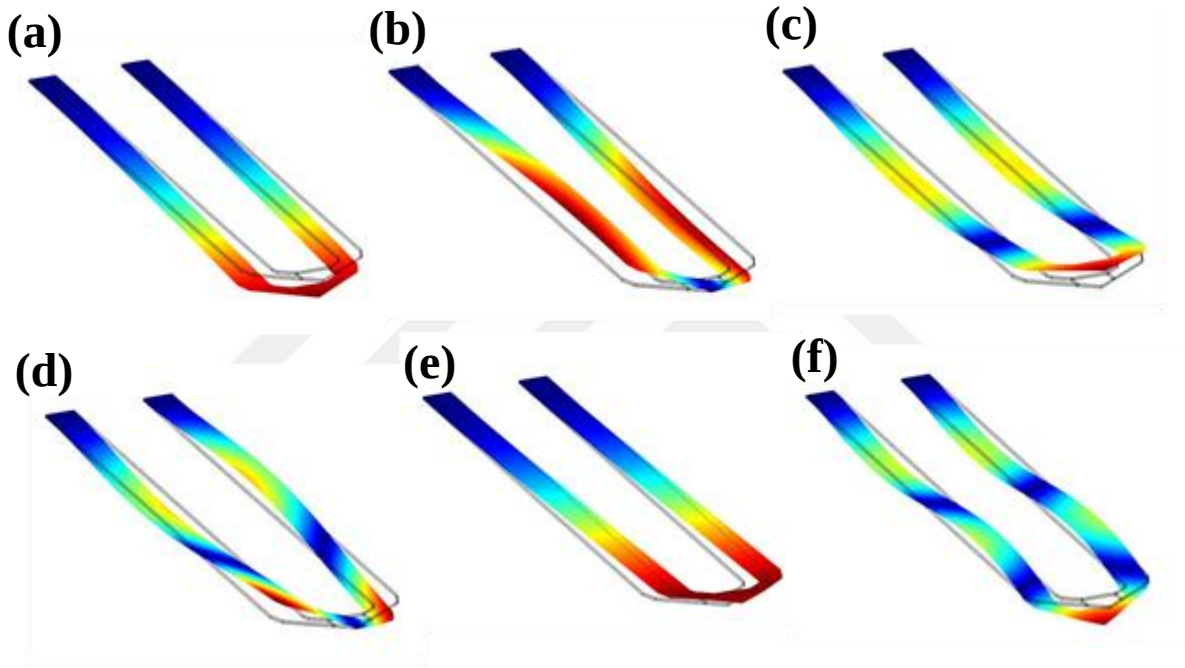

Figure 6.5 Eigenmode shapes of LCR cantilever in free oscillation simulated in COMSOL. 1st mode (a), 2nd mode (b), 3rd mode (c), 4th mode (d), 5th mode (e) and 6th mode (f). Only linear bending modes are later taken into account which corresponds to 1st, 3rd and 6th modes.

In Figure 6.5, it is demonstrated eigenmode shapes of LCR cantilevers simulated in free-oscillation. Even though different eigenmode behaviors are observed, we place importance to linear bending modes since the homogenous beam theory is only capable to explain that transverse motion. So, the linear bending corresponding a, c and f in the figure are taken into account which are also numerated as 1st, 2nd and 3rd linear bending modes.

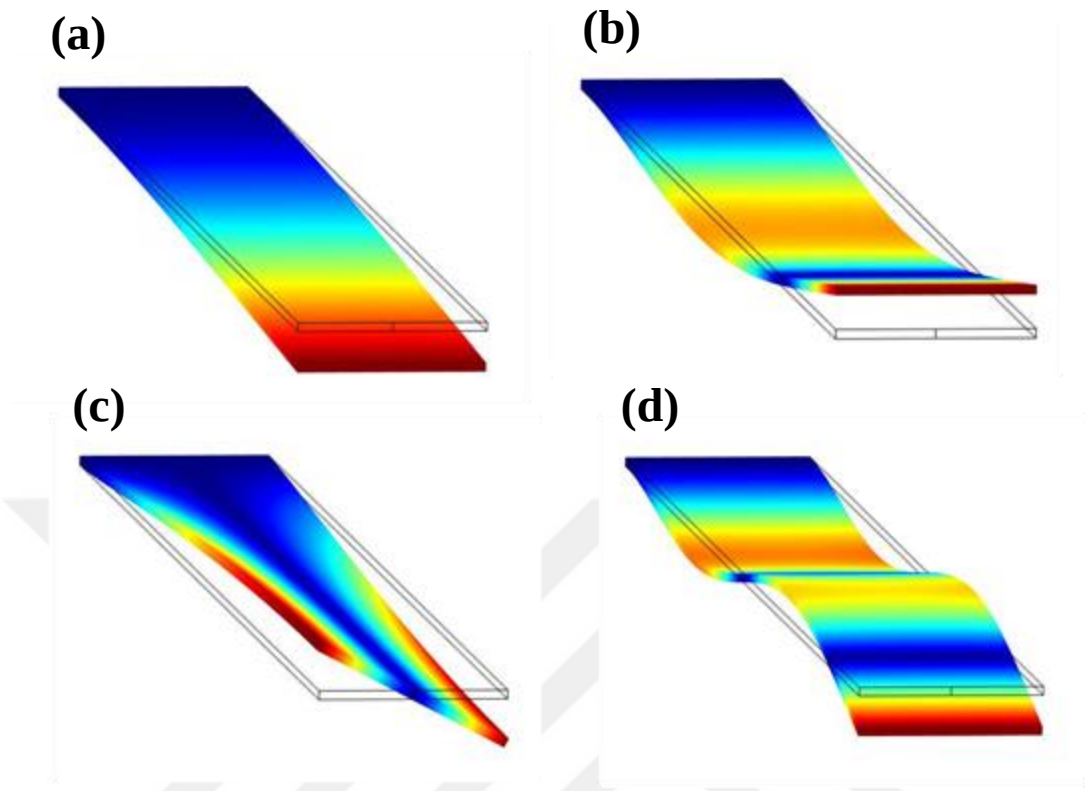

Figure 6.6 Eigenmode shapes of rectangular beam model in free oscillation simulated in COMSOL 1st mode (a), 2nd mode (b), 3rd mode (c) and 4th mode (d). Only linear bending modes are taken into account which corresponds to 1st, 3rd and 4th modes.

In Figure 6.6, eigenmode shapes of rectangular beam mode are simulated. It is clear that only linear and torsional modes shapes are obtained. As discussed above, only linear modes are considered which correspond to a, b and d of the figure. These modes are numerated as 1st, 2nd and 3rd linear bending modes of the rectangular beam model. Comparisons of linear bending eigenmode frequencies for LCR and rectangular beam model are provided in Figure 6.7. Clearly, 1st mode is exactly the same for both shapes, yet there is very small difference is observed in the 2nd mode. Also, it is quintessential that these 1st and 2nd modes having close numbers have exactly the same eigenmode shape. So, it can be confidently said that the rectangular beam model is capable of replacing LCR cantilevers considering stiffness and 1st and 2nd free oscillation eigenmodes.

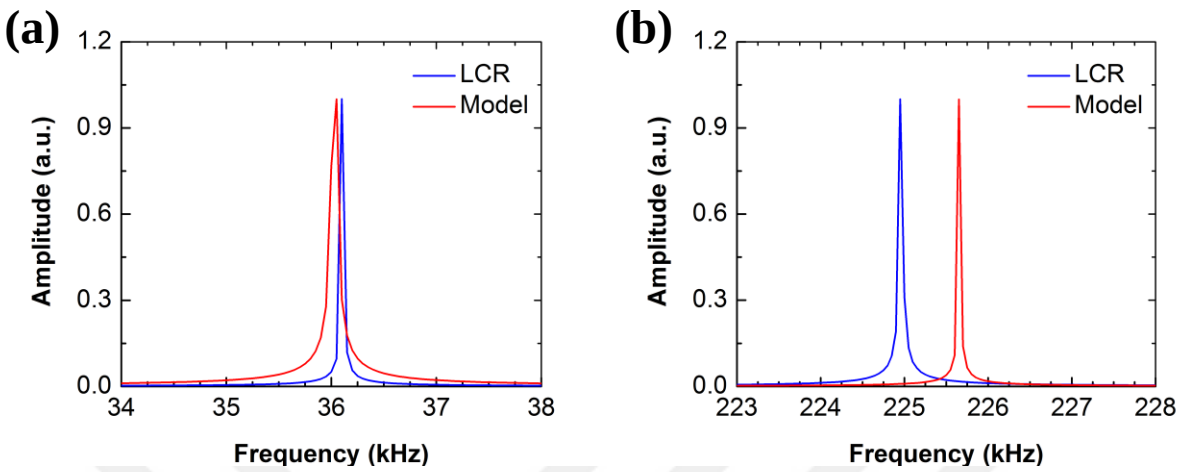

Figure 6.7 Eigenmode frequency comparisons of LCR cantilever and rectangular beam model in free-oscillation. 1st mode (a) shows almost matching frequencies for both forms. 3rd mode (b) yields very slight difference between the model and the LCR cantilevers.

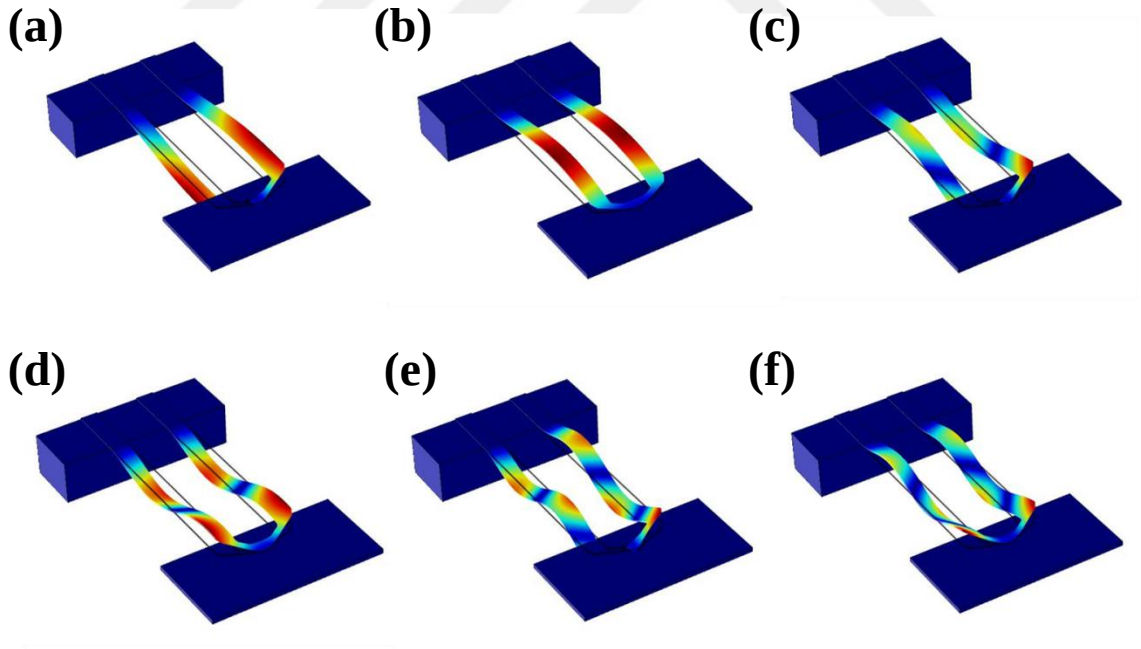

Figure 6.8 Eigenmode shapes of LCR cantilever in contact resonance simulated in COMSOL. 1st mode (a), 2nd mode (b), 3rd mode (c), 4th mode (d), 5th mode (e) and 6th mode (f). Only linear bending modes are later taken into account which corresponds to 2nd, 4th and 6th modes.

In Figure 6.8, it is demonstrated eigenmode shapes of LCR cantilevers simulated in contact resonance. Even though different eigenmode behaviors are observed, we place importance to linear bending modes since the homogenous beam theory is only capable to explain that transverse motion. So, the linear bending corresponding b, d and f in the figure are taken into account which is also numerated as 1st, 2nd and 3rd linear bending modes.

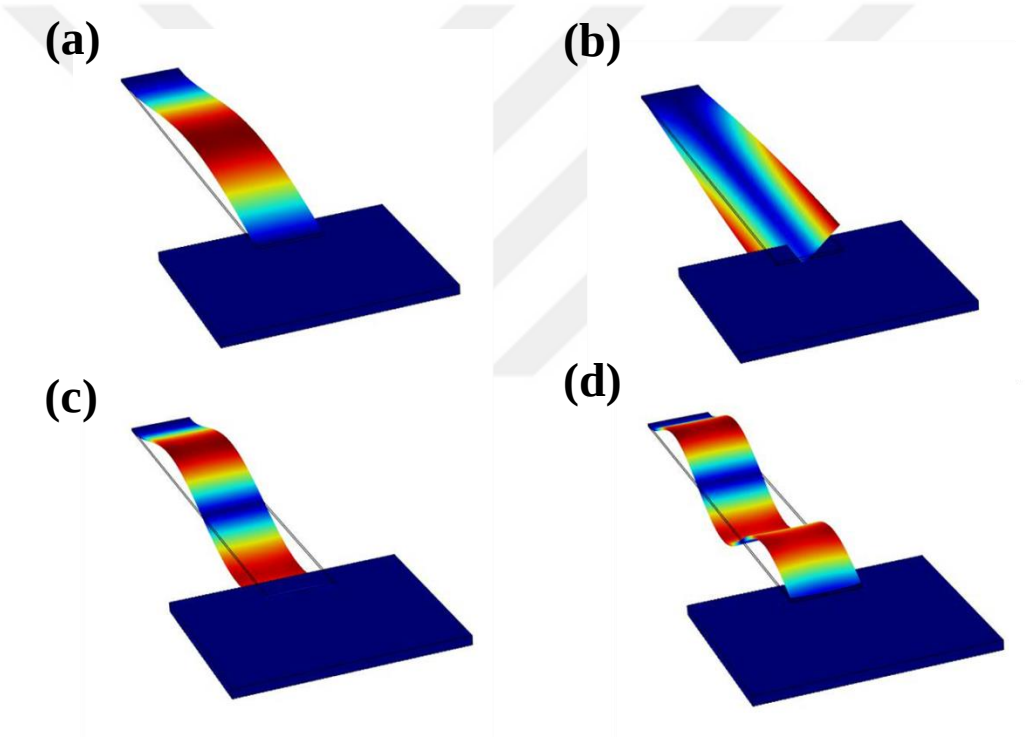

Figure 6.9 Eigenmode shapes of rectangular beam model in contact resonance simulated in COMSOL 1st mode (a), 2nd mode (b), 3rd mode (c) and 4th mode (d). Only linear bending modes are taken into account which corresponds to 1st, 3rd and 4th modes.

In Figure 6.9, eigenmode shapes of rectangular beam mode are simulated in contact resonance. It is clear that only linear and torsional modes shapes are obtained. As discussed above, only linear modes are considered which correspond to a, b and d of the figure. These modes are numerated as 1st, 2nd and 3rd linear bending modes of the rectangular beam model. Comparisons of linear bending eigenmode frequencies for LCR and rectangular beam model are provided in Figure 6.9. It can be easily said that 1st mode of the contact resonance for both LCR and the rectangular beam mode exactly match. When this finding is combined with the previous results, it is deducted that the rectangular model can be used to re-model LCR cantilevers only for the 1st eigenmode having almost equal stiffness. This finding offers a promising conclusion to be put into practice for further analyses in the future works.

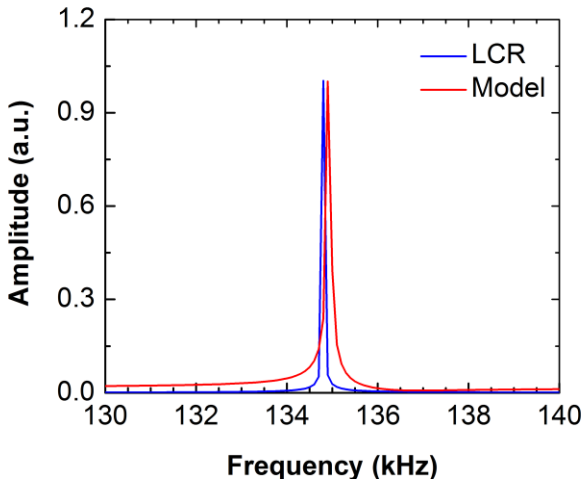

Figure 6.10 1st Eigenmode frequency comparisons of LCR cantilever and rectangular beam model in contact resonance. 1st mode shows almost matching frequencies for both forms.

CHAPTER 7: BLOCK COPOLYMER SPECTROSCOPY

7.1 Viscoelastic Characterization of Block Copolymers

Block copolymers have been placed increasing attention by the time that many successful works have been produced utilizing numerous block copolymer morphologies. Also, block copolymers are currently being pronounced as an emerging material for both scientific advancements and technological developments. There has been demonstrated plethora of applications of BCPs spanning nanomanufacturing [34], photovoltaic technologies [35], nanomedicine [36] and membrane technologies [37]. However, so far only a little information has been revealed regarding structural reliability and viscoelastic behaviors of the BCP morphologies. This is quite an important issue since BCP are designed for numerous applications which are expected to be operated continuously under various conditions. In this sense, a few works have been reported for mechanical characterization of BCP morphologies. They have either applied Force-Distance Curves [38] or implemented Amplitude Modulated Atomic Force Microscopy (AM-AFM) technique [39]. Yet, there is an immediate lack of providing extensive nanomechanical property maps of characteristic material properties on different types of BCP morphologies. Besides, when considered viscoelastic property analyses, any work have not been produced providing local temperature dependent viscoelastic material property measurements. It is due to the fact that state-of-the-art technologies e.g. DMA, CR-AFAM are not incapable of performing nano-scale temperature dependent measurements since they are used either for macroscopic measurements or mechanical property measurements. Hence, here we are presenting a technique, Lorentz contact resonance AFM, to provide reliable information regarding both mechanical and thermophysical measurements on the nanoscale.

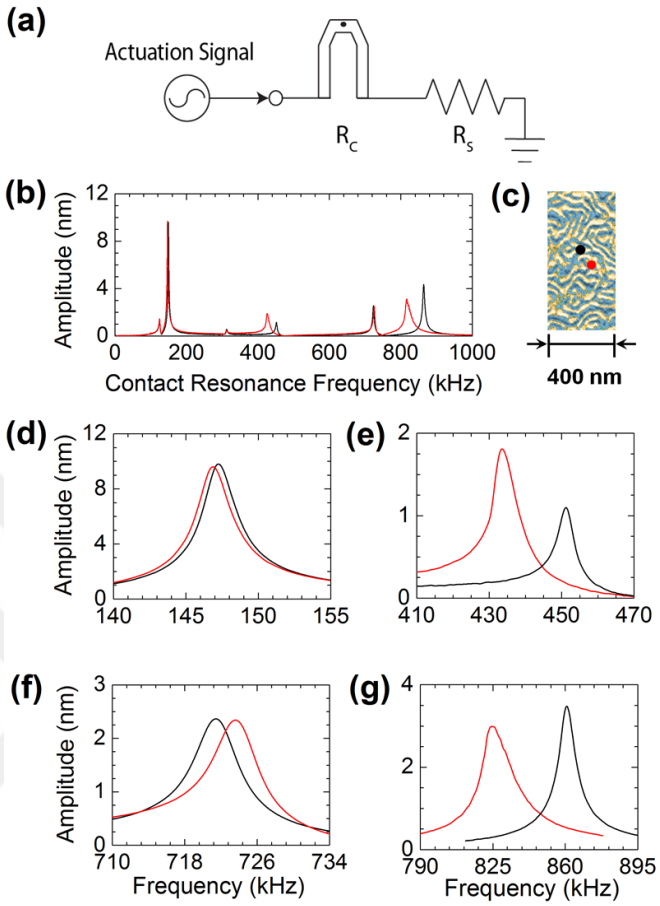

Figure 7.1 Lorentz contact resonance spectroscopy measurements taken on 37-37K PS-PMMA lamellar block copolymer sample. Lorentz actuation is provided through external AC source (a). In wide-range spectroscopy (b) four eigenmodes are observed as measurements taken PS and PMMA domains (c). 1st (d), 2nd (e), 3rd (f) and 4th (g) are analyzed to compare behaviors PS and PMMA domains.

In Figure 7.1, it is demonstrated Lorentz frequency spectra taken on 37-37K PS-PMMA lamellar morphology block copolymer sample. Red and black lines describe material responses of PMMA and PS, respectively. When individual eigenmodes are analyzed, it is observed that very slight contact resonance difference in the 1st eigenmode. Also, by increased degree of the eigenmodes, distances between the peaks get enlarged due to elevated sensitivity of higher eigenmodes. However, the 3rd mode yields almost exact contact resonance frequency values which is attributed to torsional behavior of that eigenmode.

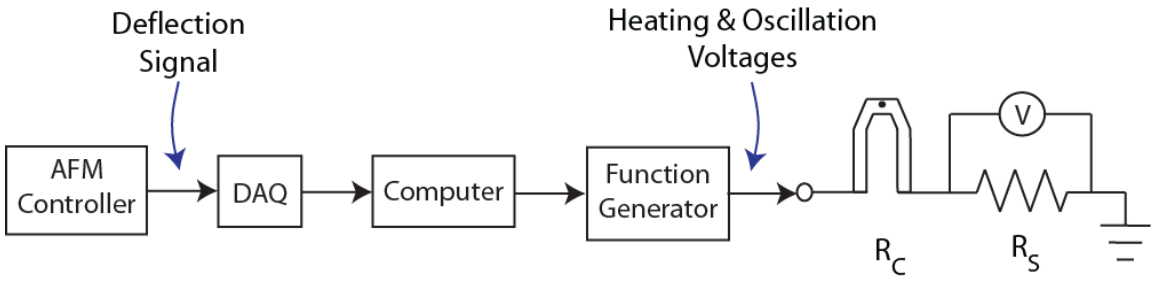

Figure 7.2 Experimental setup of LCR-AFM. The system is controlled through a Labview code on a computer. A chirp AC waveform and ramping DC voltage are sent to the cantilever. Deflection signals are collected by a DAQ board to be then transformed into frequency signal forms using FFT. Voltage drop across the sense resistor is measured to detect cantilever resistance.

We have performed local viscoelastic material property measurements on 66-63K lamellar morphology PS-PMMA block copolymer using the experimental as shown in Figure 7.2. It is achieved to acquire independent measurements on both the domains within the structure.

In Figure 7.3, it is demonstrated viscoelastic measurements taken on PMMA domains. In most of the experiments it is observed that the indentation crater left on the sample can be measured as 100 nm in diameter and 20 nm in depth. In figures a and b, there are shown a picture of indentation crater on the sample and cross-section of hole profile, respectively. After that, we have measured change of indentation diameter and depth as functions of temperature so that later we can estimate reduced elastic modulus. There is obtained quasi-linear behaviors for both the responses of diameter and depth as shown in figure c. Then, we have measured contact resonance frequency as a function of temperature while the cantilever is heated and oscillated in contact simultaneously. The contact resonance frequency has an increasing trend up to certain values then peaks and starts decreasing. The data of contact resonance frequency is later used to derive reduced elastic modulus of the material using pre-defined mathematical model and

relevant equation. It is noteworthy that the decreasing trend of the reduced elastic modulus is obtained through use of the increased size of the contact region. Finally, loss tangent of the material is obtained as a function of temperature. In Figure 7.4, it is demonstrated viscoelastic measurements taken on PS domains. In most of the experiments it is observed that the indentation crater left on the sample can be measured as 70 nm in diameter and 6 nm in depth. Same procedure as explained in great detail above is valid for this domain of BCP.

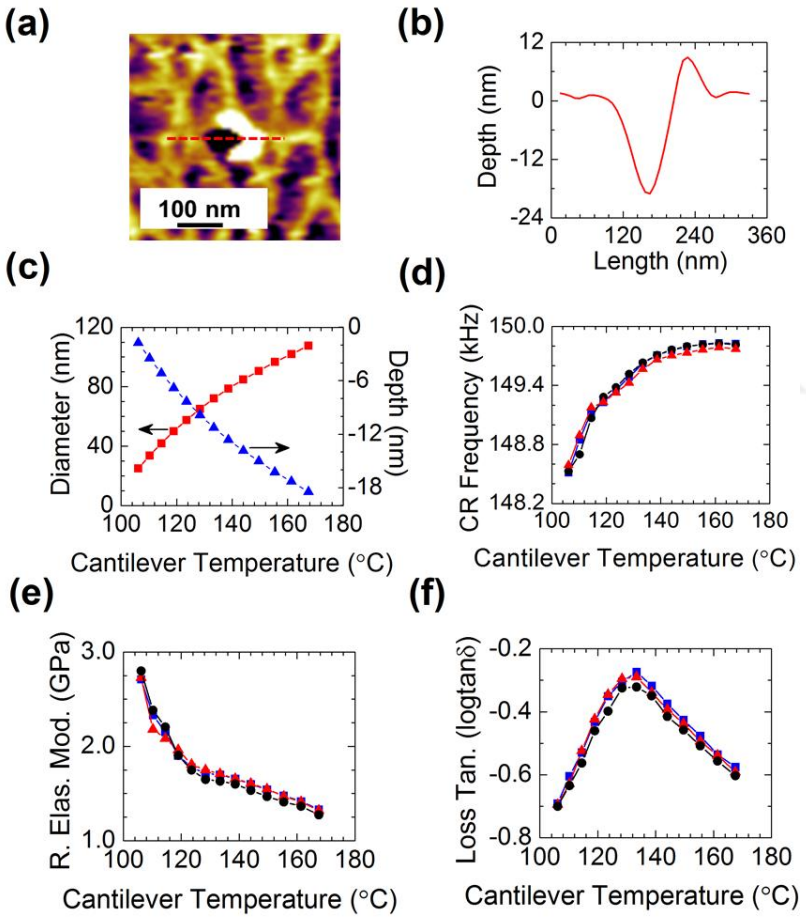

Figure 7.3 Local viscoelastic analyses of PMMA domains 66-63K PS-PMMA. Indentation crater (a) with cross-section (c) are demonstrated. Changes of indentation depth and diameter as functions of temperature (c) are used to estimate reduced elastic modulus (e) employing contact resonance frequency (d). Also, loss tangent behavior (f) is obtained as function of temperature.

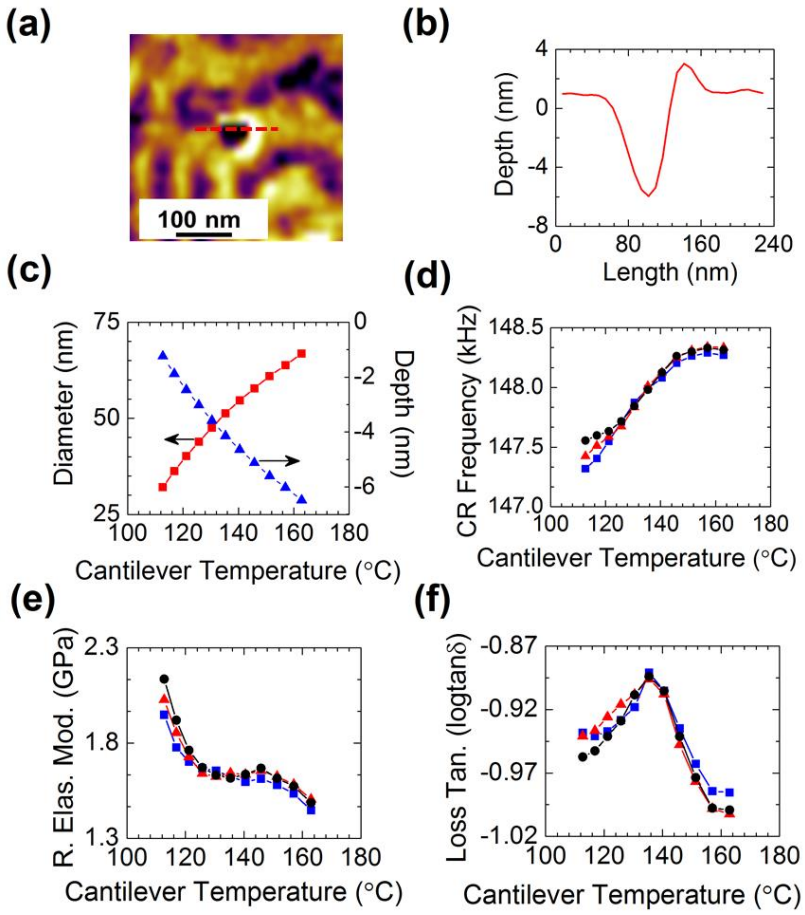

Figure 7.4 Local viscoelastic analyses of PS domains on 66-63K PS-PMMA. Indentation crater (a) with cross-section (c) are demonstrated. Changes of indentation depth and diameter as functions of temperature (c) are used to estimate reduced elastic modulus (e) employing contact resonance frequency (d). Also, loss tangent behavior (f) is obtained as function of temperature.

7.2. Surface Property Mapping of Block Copolymers

We are able to grab surface mappings of mechanical properties of block copolymer morphologies using phase-locked loop implemented atomic force microscopy, as experimental setup is shown in Figure 7.5.

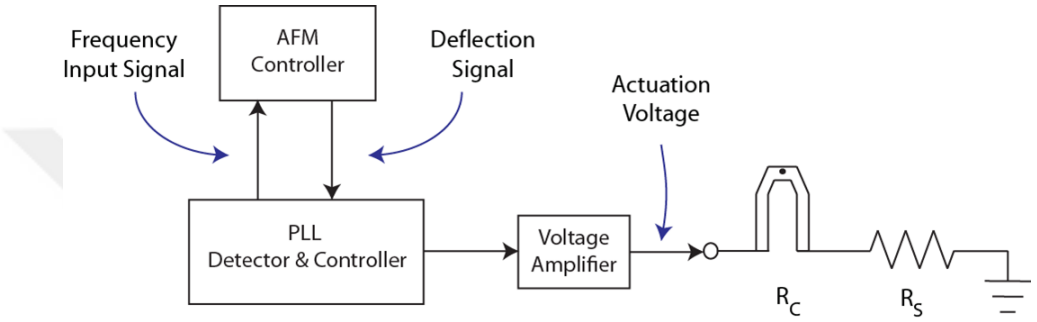

Figure 7.5 Experimental setup design for surface mappings of nanomechanical properties of PS –PMMA block copolymer samples. Oscillation frequency is automatically measured and set by PLL controller that then sends actuation voltage to first voltage amplifier and next to the cantilever. Detected deflection signal regarding that frequency is reported back to the PLL detector. Using a set phase value, changes in frequency are sent back to AFM controller as input frequency signal later to be transformed into frequency data points in obtained images.

In Figure 7.6, it is demonstrated surface maps of contact resonance frequency, contact stiffness and reduced elastic modulus for 46-21K PS-PMMA cylindrical morphology block copolymer. Two different materials, PS and PMMA, can easily be distinguished in the terms of these properties. Besides, through a cross-section taken on reduced elastic modulus map also clearly points two different values of the reduced elastic modulus for both materials. In addition, the histogram of the obtained for the elastic modulus shows two different chunks clearly having different values. Similar comments can be made for the results shown in Figure 7.7.

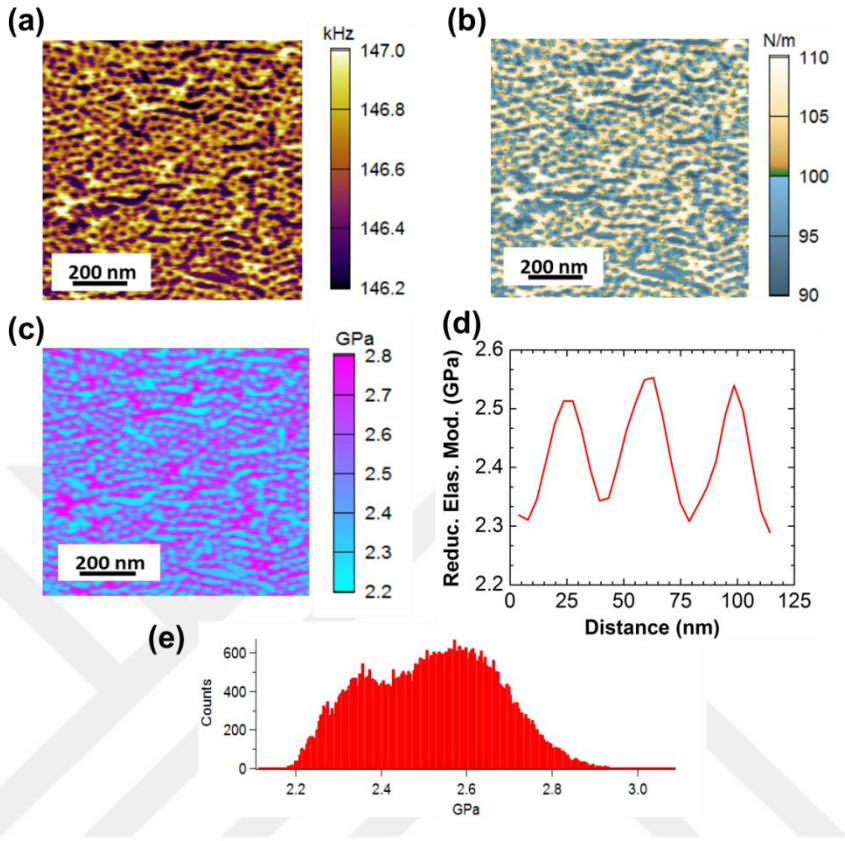

Figure 7.6 Surface nanomechanical property measurements on 46-21K PS-PMMA cylindrical morphology block copolymer samples. Contact resonance frequency map (a), contact stiffness map (b), reduced elastic modulus map (c), reduced elastic modulus cross-section (d) and histogram of the reduced elastic modulus (e) are provided.

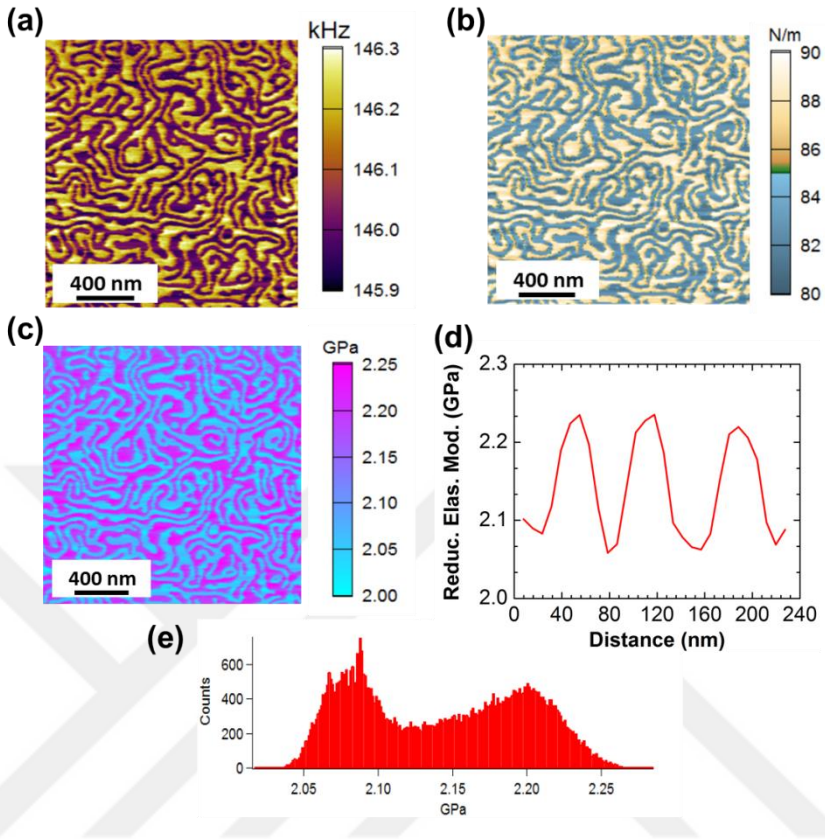

Figure 7.7 Surface nanomechanical property measurements on 37-37K PS-PMMA cylindrical morphology block copolymer samples. Contact resonance frequency map (a), contact stiffness map (b), reduced elastic modulus map (c), reduced elastic modulus cross-section (d) and histogram of the reduced elastic modulus (e) are provided.

CHAPTER 8: CONCLUSION

8.1 Applications

Viscoelastic material metrology technique developed in this study can be implemented to numerous applications in polymer science. Characterization of polymer blends, composite materials, multi-phase structures and biomedical products are pronounced among potential applications of the Lorentz contact resonance local viscoelastic property analysis method. Furthermore, the viscoelastic Lorentz technique has vast potential to replace existing thermopyhsical material characterization technologies in the near future. Being less-deformative, applicable to nano-scale domains and producing repeatable results, V-Lorentz is a promising tool to effectively be employed in research labs, industrial applications and academic purposes.

8.2 Future Work

There are several aspects that may offer a future direction to improve the local viscoelastic metrology technique presented in this work. First, the method can be employed on blends of polymers having different thermophysical properties. Second, constitutive equations can be developed to extract material properties of storage modulus, loss modulus, or hardness so that more comprehensive material characterizations can be done. Third, temperature measurements can be moved to higher order transitions such as crystallization, or melting. Fourth, the harmonic oscillator model can be upgraded for best fit with different temperature dependent responses of various materials. Last, V-Lorentz can be modified to applications of multi-frequency atomic force microscopy operations (MF-AFM).

8.3 Summary

This thesis demonstrates development of a material metrology technique for investigation of viscoelastic properties of polymer films in the glass transition region. Initially, it is demonstrated that tracking contact resonance frequency as a function of temperature can reproducibly detect glass transition temperature. Then differential increase rate of cantilever electrical resistance is monitored with respect to temperature increase. It is shown that the glass transition phenomenon happens through a slight constant regime in the electrical resistance curves. After that, differential power consumption of the cantilever is analyzed based on continuous temperature increments. It is clearly demonstrated for the first time that the glass transition temperature can be displayed with three definitive temperature points: onset, peak and end. The trend of the power consumption curves are validated by glass transition temperature measurements using Differential Scanning Calorimetry (DSC). In addition to these measurements, viscoelastic properties of the polymer in the glass transition region are investigated through implementation of harmonic oscillator model. Quality factor, contact stiffness, viscous damping coefficient and elastic modulus are monitored as functions of temperature within the glass transition region. The results are in agreement with harmonic oscillator model. Moreover, multi-frequency actuation for contact resonance is exhibited providing analyses for qualitative material properties. Also, a mathematical approach is developed to model LCR cantilevers as in the form of homogenous rectangular beam. Finally, local viscoelastic measurements taken on lamellar block copolymer film are presented. Also, nanomechanical surface property mappings of both lamellar and cylindrical block copolymer morphologies are provided.

REFERENCES

[1] G. Binnig, C. Quate, C. Gerber, Atomic force microscope, Physical Review Letters, 56 (1986) 930.

[2] U. Rabe, S. Amelio, E. Kester, V. Scherer, S. Hirsekon, W. Arnold, Quantitative determination of contact stiffness using atomic force acoustic micrsocopy, Ultrasonics, 38 (2000) 430-437.

[3] P. A. Yuya, D. C. Hurley, J. A. Turner, Contact-resonance atomic force microscopy for viscoelasticity, J. Appl. Phys., 104 (2008) 074916.

[4] B. A. Nelson, W. P. King, Measuring material softening with nanoscale spatial resolution using heated silicon probes, Review of Scientific Instruments, 78 (2007) 023702.

[5] S. Jesse, M. P. Nikiforov, L. T. Germinario, S. V. Kalinin, Local thermomechanical characterization of phase transitions using band excitation atomic force acoustic microscopy, Applied Physics Letter, 93 (2008) 073104.

[6] E. Dillon, K. Kjoller, C. Prater, Lorentz contact resonance imaging for atomic force microscopes: probing mechanical and thermal properties on the nanoscale, Microscopy Today, 21(6) (2013) 18-24.

[7] B. Nysten, C. Fretigny, S. Cuenot, Elastic modulus of nanomaterials: resonant contact-AFM measurement and reduced-size effects, Proceedings of the SPIE, 5766 (2005) 78-88.

[8] J. P. Killgore, R. M. Overney, Interfacial mobility and bonding strength in nanocomposite thin film membranes, Langmuir, 24 (2008) 3446-3451.

[9] A. V. Ruzette, L. Leibler, Block copolymers in tomorrow's plastics, Nature Materials, 4 (2005) 19-31.

[10] T. Souier, Y. A. Samad, B. S. Lalia, R. Hashaikeh, M. Chiesa, Nanoscale Thermal Analysis of Multiphase Polymer Nanocomposites, J. Phys. Chem. C 116 (2012) 8849-8856.

[11] L. Harding, W. P. King, X. Dai, D. Q. M. Craig, M. Reading, Nanoscale characterization and imaging of partially amorphous materials using local thermomechanical analysis and heated tip AFM, Pharmaceuticals Research, 24 (2007) 2048-2054.

[12] S. E. Campbell, V. L. Ferguson, D. C. Hurley, Nanomechanical mapping of the osteochondral interface with contact resonance force microscopy and nanoindentation, Acta Biomaterialia 8 (2012) 4389-4396.

[13] U. Rabe, K. Janser, W. Arnold, Vibrations of free and surfacecoupled atomic force microscopy cantilevers: Theory and experiment, Review of Scientific Instruments, 67 (1996) 3281.

[14] J. P. Killgore, D. G. Yablon, A. H. Tsou, A. Gannepalli, P. A. Yuya, J. A. Turner, R. Proksch, D. C. Hurley, Viscoelastic property mapping with contact resonance force microscopy, Langmuir, 27 (2011) 13983-13987.

[15] D. C. Hurley, M. Kopycinska-Muller, A. B. Kos, R. H. Geiss, Nanoscale elastic-property measurements and mapping using atomic force acoustic microscopy methods, Measurement Science and Technology, 16 (2005) 2167-2172.

[16] M. P. Nikiforov, S. Jesse, A. N. Morozovska, E. A. Eliseev, L. T. Germinario, S. V. Kalinin, Probing the temperature dependence of the mechanical properties of polymers at the nanoscale with band excitation thermal scanning probe microscopy, Nanotechnology, 20 (2009) 395709-395719.

[17] B. Lee, D. C. B. Prater, W. P. King, Lorentz force actuation of a heated atomic force microscope cantilever, Nanotechnology, 23 (2012) 055709-055717.

[18] D. C. Hurley, Contact resonance force microscopy techniques for nanomechanical measurements, Applied Scanning Probe Methods XI Nanoscience and Technology, (2009) 97-138.

[19] P. A. Yuya, D. C. Hurley, J. A. Turner, Relationship between Q-factor and sample damping for contact resonance atomic force microscope measurement of viscoleastic properties. J. Appl. Phys., 109 (2011), 113528.

[20] U. Rabe, S. Amelio, M. Kopycinska, S. Hirsekorn, M. Kempf, M. Goken, W. Arnold, Imaging and measurement of local mechanical material properties by atomic force acoustic microscopy, Surf. Interface Anal., 33 (2002) 65-70.

[21] M. Kopycinska-Muller, R. H. Geiss, D. C. Hurley, Contact mechanics and tip shape in AFM-based nanomechanical measurements, Ultramicroscopy, 106 (2006) 466-474.

[22] K. Yamanaka, Y. Maruyama, T. Tsuji, K. Nakamoto, Resonance frequency and Q factor mapping by ultrasonic atomic force microscopy, Appl. Phys. Lett., 79 (2001) 1939.

[23] U. Rabe, W. Arnold, Acoustic microscopy by atomic force microscopy, Appl. Phys. Lett. 64 (1994) 1493.

[24] J. Lee, T. Beechem, T. Wright, B. Nelson, S. Graham, W. King, Electrical, thermal, and mechanical characterization of silicon microcantilever heaters, Microelectromechanical Systems, Journal of, 15 (2006) 1644-1655.

[25] B. W. Chui, M. Asheghi, S. Y. Ju, K. E. Goodson, T. W. Kenny, H. J. Mamin Intrinsic-carrier thermal runaway in silicon microcantilevers, Microscale Thermophys. Eng., 3 (1999) 217-228.

[26] M. P. Nikiforov, S. Gam, S. Jesse, R. J. Composto, S. V. Kalinin, Morphology mapping of phase-seperated polymer films using nanothermal analysis, Macromolecules, 43 (2010) 6724-6730.

[27] H. G. H. van Melick, L. E. Govaert, H. E. H. Meijer, On the origin of strain hardening in glassy polymers, Polymer, 44 (2003) 2493-2502.

[28] U. Rabe, J. Turner, W. Arnold, Analysis of the high-frequency response of atomic force microscope cantilevers, Appl. Phys. A 66 (1998) 277-282.

[29] C. T. Moynihan, Correlation between the width of the glass transition region and the temperature dependence of the viscosity of High-Tg glasses, J. Am. Ceram. Soc., 76 (5) (1993) 1081-1087.

[30] Y. P. Koh, S. L. Simon, Structural relaxation of stacked ultrathin polystyrene films, Journal of Polymer Science: Part B: Polymer Physics, 46 (2008) 2741-2753.

[31] B. J. Rodriguez, C. Callahan, S. V. Kalinin, R. Proksch, Dual-frequency resonance-tracking atomic force microscopy, Nanotechnology, 18 (2007) 475504.

[32] S. Guo, S. D. Solares, V. Mochalin, I. Neitzel, Y. Gogotsi, S. V. Kalinin, S. Jesse, Multifrequency imaging in the intermittent contact mode of atomic force microscopy: beyond phase imaging, Small, 8 (2012) 1264-1269.

[33] J.E. Sader, Parallel beam approxiamation for V-shaped atomic force microscopy cantilevers, RSI, 66 (1995) 4583.

[34] M.S. Onses, C. Song, L. Williamson, E. Sutanto, P.M. Ferreira, A.G. Alleyne, P.F. Nealey, H. Ahn, J.A. Rogers, Hierarchical patterns of three-dimensional block copolymer films formed by electrohydrodynamic jet printing and self-assembly, Nature Nanotechnology, 8(9) (2013) 667-675.

[35] M. He, F. Qiu, Z. Lin, Conjugated rod-coil and rod-rod block copolymer for photovoltaic applications, J. Mater. Chem., 21 (2011) 17039-17049.

[36] S. Mura, J. Nicolas, P. Couvreur, Stimuli-response nanocarriers for drug delivery, Nature Materials, 12 (2013) 991-1003.

[37] X. Qiu, H. Yu, M. Karunakaran, N. Pradeep, S. P. Nunes, K-V. Peinermann, Selective seperation of similarly sized proteins with tunable nanoporous block copolymer, ACS Nano, 7(1) (2013) 768-776.

[38] D. Wang, K. Nakajima, S. Fujinami, Y. Shibasaki, J-Q. Wang, T. Nishi, Characterization of morphology and mechanical properties of block copolymers using atomic force microscopy: Effects of processing conditions, Polymers, 53(9) (2012) 1960-1965.

[39] E. T. Herruzo, A. P. Perrino, R. Garcia, Fast nanomechanical spectroscopy of soft matter, Nature Communications, 5 (2014) 3126.